Solid Earth Discuss., 6, 1625–1686, 2014
www.solid-earth-discuss.net/6/1625/2014/
doi:10.5194/sed-6-1625-2014

Solid Earth Discussions
Open Access

Analogue experiments of salt flow and pillow growth due basement faulting and differential loading

M. Warsitzka[1], **J. Kley**[2], **and N. Kukowski**[1]

[1]Friedrich-Schiller-University Jena Institute of Geosciences Burgweg 11 07749 Jena, Germany
[2]Georg-August-University Göttingen Geoscience Centre Department of Structural Geology and Geodynamics, Goldschmidtstr. 3 37077 Göttingen, Germany

Received: 23 June 2014 – Accepted: 25 June 2014 – Published: 17 July 2014

Correspondence to: M. Warsitzka (michael.warsitzka@uni-jena.de)

Published by Copernicus Publications on behalf of the European Geosciences Union.

Abstract

Basement faulting is widely acknowledged as a potential trigger for salt flow and the growth of salt structures in salt-bearing extensional basins. In this study, dynamically scaled analogue experiments were designed to examine the evolution of salt pillows and the kinematics of salt flow due to a short pulse of basement faulting and a long-lasting phase of successive sedimentation. ~~Experiments performed in the framework of this study consist of~~ viscous silicone putty ~~to~~ simulate ductile rock salt, and a PVC-beads-quartz sand mixture ~~representing~~ a brittle supra-salt layer. In order to derive 2-D incremental displacement and strain patterns, the analogue experiments were monitored by an optical image correlation system (Particle Imaging Velocimetry). By varying layer thicknesses and extension rates, the influence of these parameters on the kinematics of salt flow were tested. Model results reveal that significant strain is triggered in the viscous layer by minor basement faulting. During basement extension downward flow occurs in the viscous layer above the basement fault tip. In contrast, upward flow takes place during post-extensional sedimentation. Lateral redistribution of the viscous material during post-extensional sedimentation is associated with subsidence above the footwall block and uplift adjacent to the basement faults leading to the formation of pillow structures (primary pillows). Decoupled cover faulting and the subsidence of peripheral sinks adjacent to the primary pillow causes the formation of additional pillow structures at large distance from the basement fault (secondary pillows). Experimental results demonstrate that the development of salt pillows can be triggered by basement extension, but requires a phase of tectonic quiescence. The potential for pillow growth and the displacement rate in the viscous layer increase with increasing thickness of the viscous layer and increasing extension rate, but decrease with increasing thickness of the overburden. The experimentally obtained structures resemble those of some natural extensional basins, e.g. the North German Basin or the Mid-Polish Trough, and can help to understand the kinematics ~~during the~~ structural evolution.

SED
6, 1625–1686, 2014

1 Introduction

Generally, rock salt behaves as a viscous fluid even under low confining pressure and low temperatures (Urai et al., 2008; van Keken et al., 1993). Salt flow is mainly driven by a hydraulic pressure gradient, which depends on the sum of elevation head and pressure head (Kehle, 1988; Hudec and Jackson, 2007). In the case of basement extension (Fig. 1a), a hydraulic head within a salt layer is implemented by (1) vertical displacement of the salt layer itself, (2) decoupled faulting of the overburden (displacement loading), and (3) sedimentary differential loading due to sedimentation (e.g. Geil, 1991; Hudec and Jackson, 2007; Jackson et al., 1994; Jackson and Vendeville, 1994; Koyi et al., 1993; Koyi and Petersen, 1993; Remmelts, 1995; Stewart et al., 1996; Vendeville et al., 1995).

Previous dynamically scaled analogue experiments that focussed on deformation within the viscous layer above an active basement fault mostly used coloured analogue material to reconstruct the deformation history from finite structures. It has been shown that salt flows towards the hanging wall block under sediment-starved conditions. In contrast, reverse flow towards the footwall block occurs, if sufficient sediment accumulates in the depocentre above the downthrown basement block (Jackson et al., 1994; Koyi et al., 1993; Nalpas and Brun, 1993; Ge and Vendeville, 1997). Furthermore, salt flow into a growing salt structure close to the basement fault can change through time from the footwall side during an early stage to the hanging wall side in a mature stage (Burliga et al., 2012; Koyi et al., 1993). Nevertheless, incremental strain history of the viscous material and flow kinematics in precursor diapiric evolution (Fig. 1a) in particular were never examined.

Conceptual models of salt structure evolution show that either reactive salt diapirs (e.g. Jackson and Vendeville, 1994; Stewart et al., 1996) or pre-diapiric salt pillows (e.g. Koyi et al., 1993; Krzywiec, 2004b; Trusheim, 1960) are triggered by basement faulting depending on displacement rate, layer thicknesses and absolute displacement (Fig. 1). Analogue experiments investigating basement-involved deformation of a brittle-ductile-

SED
6, 1625–1686, 2014

sequence mostly focussed on the structural development of the overburden layer and the formation of reactive diapirs. These model studies demonstrate that discrete basement faulting is balanced by decoupled and diffuse faulting and flexural bending of the overburden in the presence of a sufficiently thick ductile layer (Burliga et al., 2012; Dooley et al., 2003, 2005; Ge and Vendeville, 1997; Higgins and Harris, 1997; Jackson and Vendeville, 1994; Koyi et al., 1993; Nalpas and Brun, 1993; Oudmayer and de Jager, 1993; Richard, 1991; Soto et al., 2007; Stephansson, 1972; Vendeville, 1988; Vendeville et al., 1995; Vendeville and Jackson, 1992; Ventisette et al., 2005; Withjack and Callaway, 2000). In most of the experimental studies mentioned above, either the displacement at the basement faults or the thickness of the brittle cover layer were large compared to the thickness of the viscous layer. In contrast, conditions for the early evolution of salt structures, especially of salt pillows, in extensional basins with relatively thin pre-kinematic cover layer and small-offset basement faults have not been investigated systematically.

Both, the kinematics of salt flow and the early evolution of salt structures are crucial for the reconstruction of regional subsidence patterns and facies distribution of the post-salt sediments in extensional basins (e.g. Alves et al., 2002; Duffy et al., 2013; Frisch and Kockel, 1999; Geluk, 2005; Krzywiec, 2004a) and, therefore, help e.g. to understand the history of hydrocarbon entrapment close to or underneath salt structures.

Our experimental study addresses salt pillow formation and concomitant salt flow patterns triggered by basement normal faulting and post-extensional sedimentation. We have investigated (1) the structural evolution of the viscous and brittle layer during a short pulse of basement faulting and a long phase of post-extensional sedimentation, and (2) the incremental displacement and strain patterns in the viscous layer during experimental evolution. Furthermore, a parameter study was carried out to (3) test the role of salt thickness, cover thickness and extension rate in affecting flow patterns. A 2-D optical particle tracking system (PIV) was applied to observe incremental particle displacement and strain pattern in both, the brittle and the ductile layer during the ex-

SED
6, 1625–1686, 2014

periments. In order to mimic the conditions of early-stage salt structures in extensional basins (such as the North German Basin or the Mid-Polish Trough), we applied a low ratio of basement fault offset to viscous thickness D_r, as well as a low ratio of cover thickness to viscous thickness H_r.

2 Method and procedure

2.1 Scaling analogue experiments

The experiments presented here involve a two layer ductile-brittle system covering a rigid basement. The viscous near-Newtonian behaviour of rock salt (Urai et al., 2008, van Keken et al., 1993) was simulated by using silicone putty (PDMS, polydimethylsiloxane; dynamic viscosity of 2.3×10^4 Pa s at room temperature 20 °C and experimental strain rates of $< 10^{-1}$ s^{-1}; see Appendix A for details). The silicone putty shows a power-law viscous rheology with a low power-law stress exponent (n = 1.3; Rosenau et al., 2009) so that it can also be assumed as near-Newtonian. Frictional-plastic slip behaviour of overburden sediments is modelled by a granular mixture of quartz sand and PVC microspheres (1 : 1) (see Appendix A for details). This granulate deforms according to the Mohr–Coulomb criterion, a suitable rheology for the simulation of natural sedimentary rocks (e.g. Lohrmann et al., 2003).

For representative quantitative and qualitative information, analogue models have to be scaled geometrically, kinematically, and dynamically (Hubbert, 1937; Ramberg, 1967). This requires dimensionless ratios relating rheologies and stresses of nature to experiments to be similar. Referring to previous studies, we employ a geometric scaling factor l^* of about 10^{-5}, which means 1 cm in the model is equivalent to about 1 km in nature (Koyi et al., 1993; Nalpas and Brun, 1993; Ge and Vendeville, 1997; Withjack and Callaway, 2000; Dooley et al., 2003). Dynamical scaling is ensured if force ratios and length ratios are similar (gravitational acceleration = 9.81 m s^{-2}). The reliability of modelling results strongly depends on mechanical coupling between viscous

SED
6, 1625–1686, 2014

layer and overburden and, therefore, on the ratio between brittle yield strength S_b and ductile strength S_d (see Appendix B for a detailed description of the scaling procedure). Calculation of this strength ratio results in the following values (Table 1):

$S_b/S_d(\text{nature}) = \sim 100–1000$

and

$S_b/S_d(\text{model}) = 50–180.$

The model ratio lies within the lower range of the natural ratio. Hence, the models can be considered as dynamically scaled. Scaling of time can be achieved by dividing the viscosity ratio η^* through the normal stress ratio σ_N^* (see Appendix B). The resulting time scaling factor $t^* = \sim 10^{-10}$ means that one hour in the experiment equals ~ 1 Ma in nature.

Note that the applied scaling procedure is subject to high uncertainties, since especially salt viscosity and strain rate during salt flow are not well constrained and can vary over two to three orders of magnitude (Jackson and Talbot, 1986). Nevertheless, similar analogue materials and length ratios have been used for decades and found suitable for modelling of salt tectonic processes (see references above).

In our experiments, we used a mixture of quartz sand and PVC beads, which possess slightly lower frictional properties ($\phi \sim 27^\circ$), but also a lower bulk density ($\rho_b = 1300\,\text{kg m}^{-3}$) than pure quartz sand ($\rho_b = 1580–1710\,\text{kg m}^{-3}$), (see Appendix A). By applying a low density contrast between cover and viscous layer in our experiments ($300\,\text{kg cm}^{-3}$), buoyancy forces are not overestimated (Allen and Beaumont, 2012). Thus, we intend to ensure a more realistic stress relation during early stages of salt pillow development, and closer similarity to natural shallow (~ 1000 m), partly compacted sediments, which also possess densities lower or slightly higher than salt.

SED
6, 1625–1686, 2014

2.2 Experimental set-up

In this generic experimental study, we intend to simulate conditions of salt structure evolution ~~present~~ during the ~~first~~ onset of basement extension. In many rifts and intracontinental basins multiple extensional phases alternate with phases of tectonic quiescence as it is revealed by structural analysis or subsidence patterns (e.g. Alves et al., 2002; Jackson and Vendeville, 1994; Kockel, 2002; Mohr et al., 2005; van Wees et al., 2000). Therefore, the experimental procedure applied here assumes a relatively short extensional pulse followed by a longer phase of tectonic quiescence accompanied by sedimentation.

Appropriate experimental values for e.g. layer thicknesses, displacement of the basement faults or the duration of extension are adapted to the conditions of the Central European Basin system, which contains prominent extensional segments (e.g. Central Graben, Horn Graben, Mid-Polish Trough) (Ziegler, 1982) and numerous salt structures (Maystrenko et al., 2013). Here, the pre-extensional overburden thickness h_b varies from a few hundred meters (Mid-Polish Trough; Krzywiec, 2004a) to ~ 1000 m (North German Basin; Baldschuhn et al., 2001; Maystrenko et al., 2013; Scheck et al., 2003). The maximum original salt layer thickness h_d in the centre of extensional basins mainly lies between 1000 m (Northeast German Basin) and 1500 m (Mid-Polish Trough), but can attain 3500 m (Central North German Basin; Frisch and Kockel, 1999; Maystrenko et al., 2013). Hence, a ratio of overburden thickness to salt thickness of $H_r < 1$ is a reasonable assumption. During early development of extensional basement faults and salt structures, basement fault off-set d can also be assumed to be comparatively small, i.e. values of < 1000 m. Thus, the ratio D_r of basement fault off-set to thickness of the salt layer also ranges from 0.5 to 1.

Experiments were performed in a 90 cm × 20 cm wide glass-sided box (Fig. 2a). The rigid base is subdivided into 3 blocks by two opposite planes dipping 60°. The right block is fixed, the middle one subsides controlled by an engine and the left one is free to move horizontally. The left block is wider in order to investigate the post-extensional

SED
6, 1625–1686, 2014

model evolution at distance from the basal faults. The initially planar base is covered with a flat layer of silicone putty as well as a pre-kinematic granular layer (Fig. 2b).

Each experiment starts with a displacement of the basal plate (extensional phase), whereby the middle block is pulled down d =~ 6–7 mm (Fig. 2c), which causes ~ 7 mm horizontal stretching of the whole model (~ 0.8 %). The displacement rate e on the normal faults of the basal plate ranges from 0.6, 4 to 20 mm h^{-1}, which represents a natural extension rate of 0.05 to 2 mm a^{-1} (50 to 2000 m Ma^{-1}). According to our scaling, the duration of the extensional phase (0.3 to 10 h) is about 0.3 to 11 Ma, which are reasonable values for a short extensional pulse, as it occurred e.g. in the North German Basin (e.g. Kockel, 2002). After termination of basal displacement, particle movement was monitored for several minutes (post-extensional phase) in order to record the strain patterns, but without allowing large amounts of deformation in the viscous layer (< 1 mm). After this interim period additional sand (post-extensional layers) was sieved into topographic depressions to mimic sediment aggradation (Fig. 2d) (syn-sedimentary phase). The sieving procedure was repeated every day. The average sedimentation rate was ~ 5 mm d^{-1} depending on the depth of the depressions. This rate represents a natural sedimentation rate of ~ 0.002 mm a^{-1} (~ 20 m Ma^{-1}), which is one order of magnitude lower than the average extension rate. Since we intended to investigate post-extensional structural evolution with realistic initial density contrasts, the syn-sedimentary phase lasted much longer than the extensional phase (> 5 days equivalent up to > 100 Mill. years in nature). In nature, sediment compaction would lead to an increase of the cover density and, therefore, to a faster growth of the salt structures during (see discussion).

In total, 12 experiments were carried out (Table 2). In order to examine sensitivity on the boundary conditions and reproducibility of the experiments, a reference experiment with equal initial conditions was repeated 4 times (Exp. 1a–d). The early phase was identical for these four experiments, although some variations were introduced at a later stage. In Exp. 1b, an additional phase of basal displacement was applied after 10 days. In Exp. 1c ~ 0.5 cm of sand was removed from surface after 10 days in order

SED
6, 1625–1686, 2014

to simulate erosion. Exp. 1d was terminated earlier to observe intermediate structures. In additional experiments (Exp. 2–8) initial parameters (layer thicknesses and displacement rates) were changed systematically to test their influence on structural evolution and kinematics (Table 2). In Exp. 4b, sand accumulation was applied simultaneously with displacement of the basal plate.

We used coloured sand layers to track the structural evolution. On the basis of digitized photographs of cross-sections, the final structures were sequentially restored using a vertical-simple shear restoration algorithm (Rowan and Ratliff, 2012) in 2-D Move (Midland Valley). Furthermore, 3-D models were constructed in 3-D Move (Midland Valley).

A computer-based displacement data analysis (particle imaging velocimetry, PIV) tool provided by StrainMaster© (La Vision GmbH, 2002) was used to monitor incremental strain in the granular and viscous layers, respectively, during the experiment. PIV is an optical, non-intrusive method for particle tracking consisting of digital 12 bit monochrome CCD (charge-coupled device) cameras (4 Mega Pixel; $\sim 20\,\text{pixels}\,\text{cm}^{-1}$) and analysis software (LaVision 7.0). Images were recorded every minute during basement extension and every 3 min during the syn-sedimentary phase, which is sufficient to follow deformation under low experimental strain rates. The images were processed with a cross-correlation algorithm calculating translation and distortion of textural differences (i.e. grey values) between two sequential images with a predefined time difference (Adam et al., 2005). Depending on the optical resolution of the cameras and the precision of the cross-correlation algorithm used, a spatial resolution < 0.1 pixels can be achieved (Adam et al., 2005). The resulting accuracy of the displacement vector is $\delta d = \sim 0.05$ mm for an assumed box width of 90 cm. On the basis of the calculated incremental vector displacement field, cumulative displacement, x- and y-component of displacement or strain tensor components (e.g. normal strain ε_{xx}, and shear strain ε_{xy}) as well as long-term average flow velocities u can be calculated. To achieve a textural pattern in the transparent silicone, it was blended with a small amount of sand particles

SED
6, 1625–1686, 2014

(∼ 10 g sand per 1 kg silicone). The effect of this impurity on density or viscosity of the silicone is negligible (Boutelier et al., 2008; Warsitzka et al., 2013).

All experiments were monitored in 2-D side-view, except for Exp. 1d, which was additionally recorded in 2-D top-view to observe horizontal deformation on the sand surface. For analysis of flow kinematics, the horizontal displacement d_x in side-view or normal strain ε_{xx} in top-view was used. 2-D top view visualizes horizontal extensional ($+\varepsilon_{xx}$) or compressional strain ($-\varepsilon_{xx}$). This strain can be initiated for instance by thin-skinned extension of the sand cover (Fig. 3a). Furthermore, flexural bending of the sand produces extensional, as well as compressional domains at the sand surface (Fig. 3b). Similarly, it is possible to identify uplifting and subsiding areas in the sand layer due to silicone flow (Fig. 3c). Strain distribution in a folded layer is characterized by crestal stretching ($+\varepsilon_{xx}$) of the sand surface in anticlines, whereas synclinal bending is associated with compressional strain ($-\varepsilon_{xx}$) (Schultz-Ela and Jackson, 1996).

Strain monitoring with PIV is non-intrusive (Adam et al., 2005). Hence, only the strain at the model surface can be observed. This restricts monitoring of movement in the silicone, which is constrained by friction on the glass wall boundaries and, therefore, not plane-strain. Thus, displacement observed at the glass wall is merely a fractional amount of displacement, which takes place in the middle of the box (Warsitzka et al., 2013). We reduced the effect of lateral friction of viscous material on the glass walls by lubricating the glass with a thin film of glycerine, allowing the silicone to slip along the side walls during extension.

3 Experimental results

3.1 Structure of the pillows

Cross-sections through the centre of the box of reference experiments 1a and 1b (Fig. 4a and c) show the characteristics of the final structures obtained after 12 days or 18 days, respectively. Above the downthrown hanging wall basement block, a periph-

SED
6, 1625–1686, 2014

eral sink with thickened sand layers developed, which is here called hanging wall peripheral sink (HPS). The HPS is bounded by two pillows at several centimetres distance from the basement faults. The post-extensional sand layers (red/white; blue/white) pinch out towards the crests of the two pillows causing a bowl-shaped structure of the HPS. The width of the HPS is larger than the width of the underlying basement graben. The silicone beneath the HPS is depleted, which brings the base of the sand in contact with the basement fault tips.

Two types of pillow-like structures can be distinguished in the experiments. The first (primary pillows) are situated adjacent to the basement fault above the footwall block. The second type (secondary pillow) is located further away on the footwall platform. Depth maps of the top of the viscous layer (Fig. 4b and d) reveal that the pillows are roughly 10 to 15 cm wide and their crests are raised approximately 1 cm above the initial silicone layer top. The pillows are elongated and their long axes trend parallel to the basement offset. An additional peripheral sink containing thickened post-extensional layers is located between the left-hand primary pillow and the secondary pillow. We refer to this region as footwall peripheral sink (FPS).

In Exp. 1b the basement was displaced a second time, which is marked by the blue/white layers. Here, the pre-kinematic sand layer (yellow) displays minor faulting at the crest of the pillows. Post-extensional layers of the first phase (red/white) are bent upward.

3.2 Experiment evolution

The structural evolution of Exp. 1b is illustrated by means of sequential cross-sections of restored post-extensional sand layers (Fig. 5). During the first syn-extensional stage, a small depression (HPS) forms due to subsidence of the central basement block (Fig. 5a). The cover layer above each fault tip is bent into a monocline roughly 5 cm wide. Horizontal extension in the cover layer is mainly balanced by peripheral cover grabens at the left edge of the box. These cover grabens are located close to the region, where the silicone pinches out due to a basement wedge. During the syn-sedimentary

SED
6, 1625–1686, 2014

stage, surface depressions were filled by adding sand. The first post-extensional sand layer (orange) represents the surface subsidence due to basement displacement. Successive growth beds (red-white) reflect downwarping due to flow of the viscous material. After several phases of sand accumulation, the HPS widens significantly (Fig. 5b). Areas of maximum sand accumulation gradually move from the center of the HPS towards the pillow crests. The monoclines, which formed due to basement displacement turn into anticlinal pillow structures. On the outer side of the left-hand primary pillow, an additional peripheral sink (FPS) develops. Eventually, a secondary pillow evolves above the left footwall block (Fig. 5c).

During the second phase of extension with additional 6 mm of displacement along the basement faults (Fig. 5d), the HPS reveals increased subsidence. The base of the HPS sinks onto the basal plate, which leads to a contact with the tips of the basement faults. Consequently, no additional silicone is expelled from the hanging wall side and the depocentres move closer to the crests of the pillows (Fig. 5e). The post-extensional layers of the first phase are bent upward adjacent to the pillow structures. During successive post-extensional sand accumulation (blue-white), the pillow structures become more pronounced and elevated (Fig. 5e). Although the cover is faulted at the left edge of the box, the secondary pillow starts to raise slowly at the beginning. With increased subsidence of the footwall peripheral sink, growth of the secondary pillow accelerates.

4 Displacement and strain patterns

~~By means of PIV monitoring~~ ~~d~~displacements and strain patterns are visualized for the phases during basement extension, after termination of basement extension and during accumulation of post-extensional sand layers.

SED
6, 1625–1686, 2014

4.1 Syn-extensional phase

Figure 6 shows the displacement and strain patterns of Exp. 1b after 6 mm of vertical basal displacement or 1.5 h, respectively. Patterns of horizontal strain (ε_{xx}) observed in top-view of the sand surface (Fig. 6a) reveal a zone of compression ($-\varepsilon_{xx}$, blue) and a zone of extension ($+\varepsilon_{xx}$, red). Highest amounts of ε_{xx} are accommodated at a cover graben at the left side of the box in an extensional zone. Less pronounced zones of extensional strain occur adjacent to the basement faults. These zones are surrounded by two compressional zones above the edges of the hanging wall basement block. The extensional domains bordering the basement faults above the footwall blocks are the combined effect of bending of the cover (see explanation in Fig. 3) and horizontal stretching due to opposite movement in the silicone (Fig. 6b). Similarly, the less pronounced compressional domains above the hanging wall block result from layer bending.

In the side-view of Exp. 1b, horizontal displacement d_x illustrates the lateral movement of the left basement block (Fig. 6c). The amount of d_x decreases vertically within the viscous silicone layer and virtually drops to zero in the sand layer. Hence, shearing at the base is not transmitted into the cover. Additionally, significant horizontal movement in the silicone can be recognized directly above the fault tip in a 3–4 cm wide, elliptical zone. An enlarged image (Fig. 6c and d) reveals that silicone flows towards the subsiding basement block, although the silicone layer is sheared in the opposite direction by the leftward moving basement block. The flow pattern above the fault tip can be characterized as channelized Poiseuille flow, which means that the cover layer is horizontally stable relative to the basement. In contrast, flow patterns above the leftward-moving basement block indicate a shear flow (Couette flow) above the basal plate, which decreases vertically through the silicone layer.

SED
6, 1625–1686, 2014

4.2 Post-extensional phase

After basement extension had been stopped, deformation was monitored for approximately 15 min – before the first post-extensional sand layer was added. During this interim period, patterns of the horizontal strain ε_{xx} observed in top view of Exp. 1b (Fig. 7a and b) show extensional domains (yellow) at the edges of the central hanging wall block and at the peripheral cover graben. Zones of compressional strain (blue) are identified at the edges of the footwall blocks, in the centre of the hanging wall block and adjacent to the peripheral cover graben. As explained by means of Fig. 3, extensional strains can be attributed to uplift and anticlinal bending of the thinned cover, whereas areas of compressional strain indicate subsidence and synclinal bending of the cover. Hence, the surface subsides at the edges of the footwall blocks, whereas it is uplifted at the edges of the hanging wall block. Meanwhile the peripheral cover graben is uplifted, whereas adjacent areas subside. The amount of strain (max. 0.025 %) is one order of magnitude lower than strain during the syn-extensional phase (max. 0.5 %).

The side-view of Exp. 1b (Fig. 7c) reveals flow of the viscous material towards the subsided basement block. The zones of downward flow are roughly 6 cm wide, as identified through the coloured area. Therefore, this zone is twice as wide compared to the syn-extensional stage. Only minor deformation in the silicone layer is visible at the left edge of the box. Maximum displacement d_{xmax} in the silicone ranges between 0.6 and 0.7 mm in the 15 min of this interim period. Hence, maximum displacement rates u achieved by viscous flow are 2.4 to 2.8 mm h^{-1}, which is nearly twice as high as during the syn-extensional phase ($u = \sim 1.5\,\mathrm{mm\,h^{-1}}$).

The summarizing sketch (Fig. 7d) demonstrates that the zones of silicone deflation correspond to areas of horizontal cover compression ($-\varepsilon_{xx}$) in the cover layer, while the zones of silicone inflation are related to surface extension ($+\varepsilon_{xx}$) (Fig. 7d). This indicates that down-slope silicone flux above the fault tip entails uplift above the hanging wall block and subsidence above footwall blocks. In the same way, extensional strain

SED
6, 1625–1686, 2014

observed at the peripheral cover graben denotes uplift. This suggests flow of viscous material towards the thinned cover.

4.3 Syn-sedimentary stage

One hour after filling the surface depressions, zones of extension ($+\varepsilon_{xx}$) and compression ($-\varepsilon_{xx}$) have developed (Fig. 8a). These zones are wider and the horizontal strain (ε_{xx}) is more diffuse than in the post-extensional phase. In contrast to the post-extensional phase, slight compression occurs directly above the downthrown basement block. Meanwhile, areas adjacent to the basement fault on the footwall block are characterized by extension, surrounded by additional zones of compression further outboard. The region around the peripheral cover graben at the left edge of the box displays slight extensional strain. As in the post-extensional stage, these zones of extensional strain and compressional strain can be related to surface uplift or subsidence, respectively, as illustrated in the interpretive sketch (Fig. 8b).

The displacement pattern revealed in side view (Fig. 8c) indicates that the viscous material flows from the downthrown block towards the footwall blocks. Hence, silicone is expelled from the lowered basement compartment to the raised basement compartments on both sides. The regions in the viscous layer affected by horizontal displacement are wider than in the previous phases. Furthermore, these regions are roughly twice as wide (~ 11 to 13 cm) as the monocline in the cover layer (~ 6 cm). The maximal horizontal displacement d_{xmax} in the viscous layer was approximately 0.6 to 0.7 mm during one hour of recording. Thus, displacement rates (u = 0.6 to 0.7 mm h^{-1}) were significantly lower than during the post-extensional phase (u = 2.4 to 2.8 mm h^{-1}).

Combining the observations from top view and side view, it can again be shown that the zones of silicone deflation and silicone inflation fit with areas of surface compression or surface extension (Fig. 8d). Hence, horizontal flow in the viscous layer is predominantly compensated by vertical movement in the cover layer. Material evacuation forces the cover layer to subside above the hanging wall block, while silicone inflation induces surface uplift on the footwall side of the basement step. Anticlinal up-

SED
6, 1625–1686, 2014

lift above the footwall blocks (yellow areas) eventually results in the formation of the primary pillow structures (Fig. 4). Furthermore, uplift of the peripheral cover graben continues. Nevertheless, the amount of uplift is less than during the post-extensional phase, which is a result of burial under sand in the center of the cover graben.

4.4 Subsequent sedimentation phases

During ongoing accumulation of sand, the horizontal flow pattern in the silicone layer changes gradually (Fig. 9). Initially, horizontal flow is restricted to the region above the fault tip (Fig. 9a), while solely minor displacement occurs away from the basement fault above the footwall block. Due to subsequent sand accumulation in the HPS, the zone affected by viscous flow above the fault tip widens and migrates away from the basement step towards the footwall block (Fig. 9b). After 10 days significant viscous deformation is induced away from the initial basement fault (Fig. 9c). Although the primary pillows are mainly supplied from the area above the hanging wall block, a zone of rightward (yellow) directed flow can be observed, which indicates material influx from the footwall side into the primary pillows. Furthermore, leftward directed displacement (blue) at the left edge of the box increases, which reflects material flow during increased growth of the secondary pillow. At this stage intense flow is active within the entire box. Note that at late stages, silicone flow is not plane strain anymore. Therefore, merely a part of the silicone flow can be observed at the glass wall boundary.

4.5 Second phase of extension

After 11 days, a second phase of extension with 6 mm of displacement was applied in reference experiment 1b. ~~Overall,~~ displacement patterns during this second extensional phase are similar to those observed in the first extensional phase (Fig. 10). Nevertheless, small differences are apparent. During basement extension, absolute displacement in the silicone layer above the fault tip is higher in the second phase than in the first phase, which indicates higher displacement rates in the silicone. During the

SED
6, 1625–1686, 2014

post-extensional and the syn-sedimentary phase, respectively, the lateral extent of viscous flow is smaller than during the second extensional phase. Furthermore, lateral silicone flow predominantly takes place above the footwall side. This indicates that the drainage channel in the silicone layer above the fault tip is reduced due to subsidence of the HPS.

In Exp. 1c, erosion was simulated by removing approximately 0.5 cm of sand after an experimental period of 11 days. Afterwards, PIV monitoring revealed that upward material flow continues, but absolute displacement and, therefore, displacement rates are small compared to displacement rates before erosion was applied. Subsequent sedimentary phases cause accelerated displacement.

5 Parameter study

~~Overall,~~ the structural development and flow kinematics are similar in all experiments presented ~~here.~~ However, systematic variations depending on the thickness of the viscous layer h_d, the thickness of the cover layer h_b and the basement displacement rate e can be perceived. A comparison of all experimental cross-sections and displacement patterns occurring in the specific experiments can be found in the Supplement. A summary of these flow patterns for the syn-sedimentary stage, and the maximum flow velocities in the centre of the silicone layer is presented in Fig. 11a–c. Flow velocities u were calculated for the end of the extensional stage (after 1.5 h), the end of the post-extensional stage (after 15 min), and for each syn-sedimentary phase (1 h after accumulation of sand) by dividing the maximum displacement in the centre of the viscous layer by the total time (Fig. 11a'–c'). In general, displacement rates u are highest during the post-extensional phase (u = 1 to 5 mm h^{-1}). During the syn-sedimentary phases, displacement rates are notably lower compared to the post-extensional stage (u =< 1 mm h^{-1}). Nevertheless, displacement rates increase gradually with each syn-sedimentary phase in most experiments.

SED
6, 1625–1686, 2014

5.1 Effect of basement extension rate *e*

Slower basement extension causes a wider and smoother bending of the monoclines above the fault tips (Exp. 1d, 3; Fig. 11a). A comparably narrow monocline and a small cover graben develops adjacent to the basement fault develops, if *e* is large (Exp. 2). In the other experiments (Exp. 1d, 3), the position of the cover graben is located in greater distance from the basement fault.

During the syn-extensional phase, the zone above the fault tip, which is affected by downward flow, increases in width, if *e* is small (Fig. 11a). Maximum displacement d_{xmax} in the silicone layer is significantly higher at slow basement extension (Exp. 3: $d_{xmax} = \sim 5$ mm in 495 min) than for rapid basement extension (Exp. 2: $d_{xmax} = \sim 0.5$ mm in 16 min). However, the average flow velocity *u* in the viscous layer is lower in Exp. 3 ($u = \sim 0.6\,\mathrm{mm\,h^{-1}}$) than in Exp. 2 ($u = \sim 1.8\,\mathrm{mm\,h^{-1}}$; Fig. 11a').

During the post-extensional phase and during the syn-sedimentary phase, viscous flow above the fault tip spreads over a wider zone, if basement extension was slow (Fig. 11a). By contrast, maximum displacement d_{xmax} and flow velocity *u* in the viscous layer are higher, when basement extension was rapid (Exp. 2; Fig. 11a') compared to slow basement extension (Exp. 3).

In summary, decreasing the displacement rate of the basement fault *e* leads to an increased width of the monocline in the cover, a wider zone affected by flow in the viscous layer, but a waning flow velocity in the viscous layer (Fig. 11a).

5.2 Effect of the thickness of the viscous layer h_d

A larger thickness of the viscous layer h_d causes a wider and smoother bending of the monoclines above the fault tips (Exp. 5, Fig. 11b). At small h_d (Exp. 4) a cover graben develops adjacent to the basement fault. In Exp. 4, the mature pillow structures are comparatively narrow (~ 6 cm) and are located close to the basement faults. In experiments with larger h_d (Exp. 1a, 5), pillows are wider, their elevation is higher, and the distances to the basement graben is larger (Supplement).

SED
6, 1625–1686, 2014

The zone affected by viscous flow increases in width in all phases of the experiment, if the thickness of the silicone layer is larger (Exp. 5; Fig. 11b). During basement extension, flow velocities are higher for a thick viscous layer (Exp. 5: $u = \sim 2.5\,\mathrm{mm\,h^{-1}}$) than for a thin viscous layer (Exp. 4: $u = \sim 0.7\,\mathrm{mm\,h^{-1}}$) applying an equal amount of basement extension (Fig. 11b'). A similar dependence can be observed for the post-extensional and the syn-sedimentary phase (Exp. 4: $u = \sim 0.4\,\mathrm{mm\,h^{-1}}$; Exp. 1b: $u = \sim 0.5\,\mathrm{mm\,h^{-1}}$; Exp. 5: $u = \sim 0.8\,\mathrm{mm\,h^{-1}}$). Exp. 5 ($h_b = 20\,\mathrm{mm}$; Fig. 11b') shows the highest post-extensional flow velocities of all experiments ($u = \sim 5\,\mathrm{mm\,h^{-1}}$), which even exceeds the actual basement extension rate ($e = 4\,\mathrm{mm\,h^{-1}}$). Eventually, fast silicone flux leads to an initial active piercing of the silicone through the crest of the pillow structures in this experiment.

5.3 Effect of the thickness of the cover layer h_b

A thicker cover layer h_b (Exp. 1d, 8; Fig. 11c) causes a wider and smoother bending of the monoclines above the fault tips. Compared to this, a narrow monocline occurs, if h_b is small (Exp. 6; Fig. 11c). With increasing h_b the pillows become wider and located in larger distance to the basement graben (Supplement). Only if the thickness of the cover is very large ($h_b = 15\,\mathrm{mm}$, Exp. 8), no distinct pillow structures evolve. In this case, the silicone layer above the footwall block is thickened over a broad area and the sinking of the HPS merely lasts a few syn-sedimentary phases.

Varying h_b has relatively minor effects on flow patterns. In each phase of the experiments, the lateral extent of silicone flow is only slightly wider for larger cover thicknesses (e.g. Exp. 7) compared to experiments with smaller cover thicknesses. Flow velocities u in the viscous layer are roughly similar during the syn-extensional phase, independent of h_b ($u = 1$ to $1.5\,\mathrm{mm\,h^{-1}}$; Fig. 11c′). During the post-extensional and syn-sedimentary phases, respectively, flow velocities are higher in the experiment with a thinner pre-extensional cover layer (Exp. 6) compared to experiments using a thicker cover layer (Exp. 7, 1a; Fig. 11c′).

SED
6, 1625–1686, 2014

6 Discussion

6.1 Structural evolution

Our experimental procedure involved a short pulse of basement extension, but a long lasting phase of post-extensional sedimentation, which is different from most previous experimental studies (Nalpas and Brun, 1993; Koyi et al., 1993; Dooley et al., 2005). Nevertheless, a significant structural relief in the cover layers can be observed in our experiments. Similar to Nalpas and Brun (1993) and Dooley et al. (2005) ~~in their experiments~~, we can distinguish (1) basement fault-related salt structures and (2) platform salt structures.

1. The basement fault-related salt structures, here referred to as primary pillows, are located close to the basement faults on the footwall block. Structural characteristics of primary pillows are asymmetric peripheral sinks on both sides of the pillow (hanging wall peripheral sink and footwall peripheral sink), and a relatively thin pre-kinematic overburden layer. Faults in the cover have only minor influence on these pillow structures. Instead, their shape and position are mostly controlled by the syn-sedimentary flow patterns of the viscous material, and the geometry of the preceding monocline in the cover layer. Post-extensional sand layers onlap at the flank of the monocline. Consequently, viscous material is squeezed beyond the basement fault and the primary pillows develop in lateral distance from the basement fault. This observation is in agreement with most previous experimental studies mentioned above, which showed that early stage salt structures or cover grabens are laterally decoupled from the basement fault tip, if a viscous detachment is present (e.g. Withjack and Callaway, 2000). This implies that natural salt structures, which are directly located above small-offset basement faults ($D_r <\sim 1$) were not solely triggered by this, but had to be effected by other processes, e.g. thin-skinned extension. Only if the offset of the basement fault becomes large

SED
6, 1625–1686, 2014

($D_r \gg 1$), the overburden is extended beyond the basement fault, whereas the diapir spreads above the fault tip.

2. The pillows of the second type (secondary pillows) are located further on the footwall block and related to a decoupled cover graben. We suggest that the position of secondary pillows is determined by irregularities in the basement, above which the thickness of the viscous layer changes. Therefore, natural pillows, which were triggered by thin-skinned extension, can be located directly above basement steps as it was demonstrated by other analogue experiments (e.g. Gaullier et al., 1993).

Although salt pillows may also form due to other processes, e.g. due to regional compression (Kossow and Krawczyk, 2002), due to progradation of sedimentary wedges (Ge and Vendeville, 1997), due to minibasin formation (Goteti et al., 2012; Warsitzka et al., 2013) or as a residual elevation between two salt structures (Vendeville, 2002), we present a feasible mechanism, which explains the formation of salt pillows and corresponding peripheral sinks in extensional settings. However, our experiments show that this mechanism requires a relatively thin pre-extensional salt cover layer ($h_b <\sim 1500$ m). This is only a rough quantitative estimation, since rock properties in nature (e.g. salt viscosity, strength of the overburden) are more variable than in analogue models. Generally, the potential for salt pillow growth seems to decrease significantly as soon as the ratio between thickness of the viscous layer and thickness of the cover layer H_r exceeds 1. Therefore, salt pillows showing a thicker pre-kinematic overburden layer ($h_b >\sim 1500$ m), e.g. in some parts of the North German Basin (Baldschuhn et al., 2001), were unlikely triggered by extension. These salt structures rather developed due to compressional stresses resulting from e.g. regional tectonic contraction or sediment progradation.

6.2 Kinematics

The kinematics of the flow patterns in the viscous layer before and during pillow formation can be divided into two phases: (1) syn-extensional downward flow above the

SED
6, 1625–1686, 2014

basement fault tip can be observed during the initial phase of extension (Fig. 6) and subsequent (2) upward flow during ceased basement extension and contemporaneous sediment accumulation in the hanging wall peripheral sink (Fig. 8). We interpret this interplay as a result of the prevailing direction of the hydraulic head (e.g. Kehle, 1988; Koyi et al., 1993). Downward flow is driven by elevation head. A reversal of flow direction is induced, if the pressure head exceeds the elevation head due to differential loading between the hanging wall side and the footwall side. Once upward flow is initiated, it continues until the viscous material is completely expelled from beneath the hanging wall peripheral sink into the neighbouring pillows.

In our experiments, flow velocities during syn-sedimentary upward flow are small compared to flow velocities during downward flow (Fig. 11). Hence, it can be concluded that the pressure induced by differential loading is only slightly higher than the pressure induced by elevation head. During further syn-sedimentary phases flow velocities in the viscous layer above the fault tip increase (Fig. 11) indicating a gradually increasing pressure head. The syn-sedimentary phase in our experiments lasts long (scaled to > 100 Mill. years) due to the small flow velocities in the viscous layer. In nature, differential loading may increase faster due to compaction of overburden sediments, which accelerates the growth of salt pillows.

In most experiments of this study, no sedimentation has been applied during basement extension in order to simulate two end member types of downward dominated and successive upward dominated flow patterns. In some experiments, e.g. Exp. 4b (Fig. 12), additional sand was sieved into the subsiding HPS during basement extension. In these experiments downward flow was little or non-existent, but no upward flow was induced before basement extension had been stopped. This might be due to the delay of sand addition relative to the subsidence of the hanging wall block, due to the low density contrast between the viscous material and the cover layer, and due to shearing in viscous layer above the basement fault.

In other experimental studies simulating salt diapirism due to basement extension (e.g. Burliga et al., 2012; Dooley et al., 2005) syn-extensional sedimentation had been

SED
6, 1625–1686, 2014

applied and no phase of downward flow was described. However, the density of the sand cover in those experiments was $\Delta\rho$ = 500–700 kg m^{-3} higher than the density of the viscous layer. This overstates the effect of buoyancy and differential loading (Allen and Beaumont, 2012) compared to natural systems – at least if the initial stage of the salt structure development is simulated – and enhances upward flow.

In our experiments, secondary pillows are initiated by decoupled cover faults during basement extension. The growth rate of secondary pillows is low compared to the rise of primary pillows and decreases further due to burial with post-extensional sediments. During later syn-sedimentary phases, increasing subsidence of the FPS squeezes viscous material towards both sides of the sink (Fig. 9). Hence, flow activity in the viscous material migrates away from the primary pillow and the growth of the secondary pillow is reanimated. Consequently, loading differences created by the FPS and the evolving secondary pillow are higher than loading differences due to decoupled cover extension.

In nature, there is no lateral confinement of the salt layer, which is comparable to an edge of the experimental box. Nevertheless, the pressure head decreases with increasing distance from the footwall peripheral sink. This causes a reduced strain rate within the salt layer in horizontal direction and, therefore, an accumulation of the salt close to the peripheral sink. Hence, it can be suggested that secondary pillows also may form above undeformed basement in a laterally extended salt layer. Furthermore, secondary pillows may also be generated without the occurrence of a decoupled cover graben, but exclusively due to differential loading next to a neighbouring salt structure. This process is similar to the development of "secondary diapirs", which form as a consequence of sedimentation adjacent to diapirs (Cobbold et al., 1989; Warsitzka et al., 2013) and which had been exemplarily shown to occur in nature by Strunck et al. (1998) ~~by means of~~ a natural salt pillow in the North German Basin.

6.3 Parameter study

Varying the layer thicknesses and extension rates provides insights into the conditions for pillow formation and accompanying material flow during the early evolutionary stage

SED
6, 1625–1686, 2014

of salt structures. Generally, small off-set basement faults ($D_r < 1$) may effectively trigger salt pillows, if the thickness of the viscous layer is sufficiently large and the thickness of the overburden is comparatively small.

When increasing the thickness of the viscous layer h_d, frictional forces at the vertical layer boundaries become less significant. Hence, flow rates in the viscous layer are higher in a thick salt layer than in a thin salt layer for an equal pressure gradient. This enhances the growth rate of pillows and reduces the burial or increases the erosion at the pillow crests, respectively.

Increasing the thickness of the overburden h_b enhances the brittle strength of the cover. Due to this, vertical movement of the cover is hampered and resistance against horizontal viscous flow is stronger. This decreases flow velocities and suppresses the formation of a pronounced pillow structure. Nevertheless, in our experiments widespread horizontal material flow affected the entire viscous layer in the experimental box, even if the thickness of the cover layer was large. Applying this to nature indicates that also in regions of little deformed overburden layers and basement, intense deformation can be expected in the salt layer.

The effect of basement extension rate on the final structures of the pillows is minor at least when applying small off-set basement faults as in our experimental study. Nevertheless, the basement extension rate strongly influences flow patterns and displacement rates u in the viscous layer also during the post-extensional phases. During slow basement extension (Exp. 3), the viscous material has time to flow towards the downthrown basement block and partly equilibrate the space created by subsidence as it was also observed in other experimental studies (Jackson et al., 1994; Higgins and Harris, 1997). Less syn-kinematic sediment can be added to the hanging wall peripheral sink, which reduces the effect of differential loading and, therefore, the displacement rates during upward flow. In contrast, the subsidence of the HPS is similar to basement subsidence in experiments running with fast basement extension (e.g. Exp. 2), whereby post-extensional flow velocities are higher due to higher loading differences. For natural examples, this implies that a short pulse of fast basement extension

SED
6, 1625–1686, 2014

followed by sufficiently fast accumulation in the HPS provides the best conditions for pillow growth. If sediment accumulation is too slow to keep pace with basement subsidence, the amount of differential loading remains insufficient to drive upward flow (Ge and Vendeville, 1997). If basement extension lasts longer, fast basement extension leads to hard-linked cover extension (Withjack and Callaway, 2000) and the formation of reactive diapirs (Dooley et al., 2005).

6.4 Concepts

We suggest that the temporal sequence of downward flow and subsequent upward flow in the viscous layer above a basement fault is a widespread process in natural salt-bearing extensional basins. This is because differential loading depends on variations of thickness as well as on variations of the cover density between the hanging wall and the footwall side. The density of the overburden is lower at the beginning of basement extension and increases due to compaction, if the space above the subsiding hanging wall block is continuously filled with sediments. This can be regarded as a process equivalent to increasing layer thickness above the hanging wall side in the experiments presented here. Hence, the following conceptual model is proposed for natural pillow formation (Fig. 13): at the time of initiation, a viscous layer and its brittle overburden are gradually displaced by basement faulting assuming that cover extension is partly decoupled. As long as the density at the base of the cover is smaller than that of salt, differential loading is small, even if sediment supply is high enough to keep pace with basement subsidence (Fig. 13a). Hence, downward flow is driven by elevation head. If the hanging wall basement block continues to subside, density and, therefore, differential loading increases. The pressure asserted by loading differences becomes higher than the pressure due to elevation head and upward flow is induced (Fig. 13b). If basement extension terminates, differential loading continuously drives further subsidence of the hanging wall peripheral sink and the rise of primary pillows.

Other processes may alternate with the development of salt pillows described here, e.g. the accumulation of dense sediment (such as evaporites) above the downthrown

SED
6, 1625–1686, 2014

basement block or erosion of the graben flanks. By contrast, maintaining basement extension and, therefore, increasing the amount of absolute displacement at the basement fault inevitably leads to increased cover faulting and reactive diapirism without the occurrence of a pillow stage. This has been demonstrated in other analogue experimental studies (e.g. Dooley et al., 2005; Ge and Vendeville, 1997; Nalpas and Brun, 1993). Therefore, we suggest that the formation of a pre-diapiric pillow due to basement displacement requires a phase of tectonic quiescence or at least decreased tectonic activity, but ongoing sedimentation and sediment compaction.

6.5 Comparison with natural examples

The structural development and kinematics derived from our experiments can be compared to natural examples of salt structures in extensional basins such as the Central North Sea (Duffy et al., 2013; Korstgård et al., 1993), the Dnjepr-Donez Basin (Stovba and Stephenson, 2003), the Lusitanian Basin (Alves et al., 2002), the Mid-Polish Trough (Krzywiec, 2004a; Wagner et al., 2002), the North German Basin (Baldschuhn et al., 2001; Jaritz, 1987; Kockel, 1998), the Norwegian–Danish Basin (Korstgård et al., 1993; Sørensen et al., 1998) or the Southern North Sea (Remmelts et al., 1995). Seismic cross-sections displayed in Fig. 14 show some examples of these basins. Here, salt structures and syn-kinematic peripheral sinks are situated above a faulted basement. The overburden layers of the peripheral sinks have been reconstructed using vertical simple shear (Rowan and Ratliff, 2012) and line length unfolding in 2DMove (Midland Valley). According to our experimental results, we assume that the low amount of basement extension ($D_r < 1$) during the early stage of basin evolution was insufficient to initiate diapiric structures. However, in later phases diapiric piercing could be provoked e.g. by additional basement extension, erosional unroofing of the pillows crests, or compressional squeezing (e.g. Burliga et al., 2012; Ge and Vendeville, 1997).

The salt structures exhibited in Fig. 14a and b developed above slightly deformed basement. The pillows display a close similarity to those observed in our analogue models (Fig. 4) and may represent the stage of a pre-diapiric pillow structure. In modern

SED
6, 1625–1686, 2014

literature (e.g. Hudec and Jackson, 2011), similar structures of the North German basin were interpreted as compressional anticlines. It is suggested that their overburden was too thick to allow the growth of a salt pillow. However, no phase of regional compression is reported for the time of pillow growth in the example presented here (Triassic to Jurassic). Hence, we suggest that such salt pillows are purely triggered by basement extension.

In cross-section C of the Weser Trough (North German Basin) (Fig. 14c), local thickness variations in the post-salt Middle Buntsandstein (Early Triassic) layer provide evidence for the first onset of basement faulting. During a phase of intensified extension in the Middle Keuper time (Upper Triassic) in the North German Basin (Kockel, 2002; Mohr et al., 2005; Scheck-Wenderoth et al., 2008), the HPS in the Weser Trough had increased in depth and salt pillows evolved. The crest of the pillows was already faulted at this stage. However, the cross-sectional view of experiment 1A (Fig. 4) bears a close resemblance to the pillows and the peripheral sinks in the Middle Upper Triassic. Based on our modelling results, we suggest that the main driving forces for salt flow and pillow formation were differences in loading between the peripheral sinks above the hanging wall side the locally faulted overburden above the footwall side. Due to renewed extension during Late Keuper time (Upper Triassic) and Early to Middle Jurassic reactive diapirism and subsequent passive diapir growth took place.

Extension in the Mid-Polish Trough (Fig. 14d) already started during Early Triassic or ~~maybe~~ continued since Late Permian (Krzywiec, 2004b). For this reason, the pre-kinematic (pre-extensional) overburden above Upper Permian (Zechstein) salt layer was probably very thin or completely absent. Nevertheless, the reconstruction of cross-section D suggests that no significant pillow formed before Middle Triassic. According to our conceptual model, the density of the Lower Triassic layers was insufficient to generate significant differential loading and to support an upward directed salt flow at the beginning (Early Triassic). During Middle Triassic, a second phase of basement extension and compaction of the sediments in the HPS created a pressure head, which was

SED
6, 1625–1686, 2014

high enough to drive upward flow and pillow uplift. During Late Triassic the Klodawa salt structure reached its diapiric stage due to further basement extension.

In the Lusitanian Basin (offshore Portugal) (Fig. 14e) at least three post-salt extensional pulses have been identified for Early Jurassic to Early Cretaceous (Alves et al., 2002). The initial thickness of the Latest Triassic to Early Jurassic (Hettangian) salt layer is comparatively low. Hence, salt pillows were narrow and possessed a low structural relief during Upper Jurassic. The half graben setting in this basin caused asymmetric patterns of growth strata in the HPS (Soto et al., 2007), but structurally similar salt pillows evolved above the graben highs compared to symmetric graben settings.

The cross-section in Fig. 14f presents a salt diapir located directly above a small-offset basement fault. According to our experimental results, the offset of the underlying basement fault is insufficient to trigger piercing of the overlying diapir. Hence, this salt structure was likely induced by thin-skinned extension decoupled from a basement fault zone in far distance, e.g. the Gifhorn fault zone to the west of the Bockleben diapir. The pillow evolved until the Late Triassic, when additional thin-skinned extension forced the breakthrough of the salt.

Early flow patterns within evolving salt structures cannot be retrieved from seismic interpretations, but could be proposed on the basis of our experimental results and from rare outcrop studies in salt mines. Burliga (1996) interpreted folded salt layers in a salt mine in the Klodawa salt diapir (Mid-Polish Trough) as a result of different stages of salt flow. During an early stage (lower Triassic) salt flowed downwards towards the basin axis. During the mature stage of the Klodawa diapir salt moved from the downthrown basement block towards the rising salt structure due to differential loading between the basin centre and the crest of the salt structure (Burliga, 1996). This interpretation is supported by our experimental results and shows how ~~these~~ can help to understand the evolution of salt structures and their reconstructions. Furthermore, examples from salt mines in the North German Basin disclose complex internal folding of the evaporite succession even in regions of less external tectonic imprinting in the basement or the overburden (e.g. Bornemann, 1979; Richter-Bernburg, 1980; Strozyk et al., 2013; van

SED
6, 1625–1686, 2014

Gent et al., 2010). The observation of flow kinematics in our experiments demonstrates that significant strain in the viscous layer can occur despite only slightly deformed basement and overburden.

7 Conclusions

The analogue experiments performed in this study simulate the progressive development of salt pillows and salt movement during a short phase of basement normal faulting and a long period of successive sedimentation.

1. Cross-sections of the final stages of our experiments demonstrate that considerable structural relief of the viscous layer and the overburden is created by minorly basement deformation as long as the pre-kinematic overburden layer is relatively thin, probably $h_b <\sim 1500$ m. Two types of pillow structures can be distinguished. Primary pillows are located adjacent to basement faults and encompass a peripheral sink above the down-thrown basement block. Secondary pillows develop above the footwall block at considerable distance from the basement fault. The initiation of the secondary pillow is due to thin-skinned extension, but its growth is intensified at a later stage by the rise of the primary pillow. Both types of pillow structures are mainly driven by differential loading induced by peripheral sinks above the hanging wall block or above the footwall block, respectively.

2. Monitoring the kinematics of the analogue materials with PIV reveals that significant horizontal flow is initiated in the viscous layer due to basement faulting and differential loading. During early stages of basement extension, viscous material above the basement fault tip moves downward driven by differences in elevation head. After termination of the basement extension, the pressure head due to post-extensional differential sedimentary loading forces upward flow above the basement fault. Our conceptual model for salt flow in natural extensional basins

SED
6, 1625–1686, 2014

proposes downward flow occurs, because the thickness or the density of the overburden above the hanging wall block are low during the initial stage. As soon as the depocentre above the hanging wall block is filled with additional sediments and as soon as density inversion due to compaction of the cover sediments occurs, the pressure head due to differential loading is sufficiently high to force upward flow of salt above the basement fault tip. Consequently, viscous material is squeezed out from underneath the hanging wall peripheral sink and causes the formation of pillow-like structures on the footwall side. Furthermore, our hypothesis states that the formation of salt pillows takes place during phases of post-extensional tectonic quiescence or at least phases of reduced tectonic activity, since continued basement extension would lead to thick-skinned or thin-skinned reactive diapirism.

3. Once initiated by basement faulting, viscous flow continues due to differential loading during inactive basement tectonics. Vertical movements of the overburden are compensated by horizontal movements of the viscous material. During the mature stage of the structural evolution, the zones of active viscous flow migrate away from the initial primary pillow due to deepening of the peripheral sinks. Consequently, areas far from the initial basement faults are also affected by lateral viscous flow, which initiates or enhances the growth of secondary pillows.

4. As shown by variation of first-order parameters, overall strain patterns are similar independent of layer thicknesses or displacement rates. However, the zone affected by viscous flow and the cover monocline above the fault tip are larger, if the thickness of the ductile layer h_d is larger, if the thickness of the overburden layer h_b is larger, or if the basement displacement rate e is smaller. Flow velocities in the viscous layer above the basement fault tip are larger, if the thickness of the ductile layer h_d is larger, if the thickness of the overburden layer h_b is smaller, or if the basement displacement rate e is larger. The effect of thickness variations of the ductile layer is more significant than the effect of thickness variations in the

SED
6, 1625–1686, 2014

brittle cover layer or than the influence of the extension rate. Furthermore, flow kinematics and the shape of pillows depend on absolute thicknesses of layers rather than on the ratio between both. In summary, the growth of salt pillows is most likely, if the thickness of the viscous layer is large, the thickness of the brittle overburden is small and the short pulse of basement extension occurs at high strain rates.

5. The comparison of our experimental results with natural salt-bearing extensional basins demonstrates the similarity of structural geometries, e.g. hanging wall peripheral sinks surrounded by pre-diapiric salt pillows. Despite the limitations of the experimental set-up, e.g. simple basement geometry or no syn-extensional sedimentation, our experimental procedure provides a generic model for the early evolution of salt structures in basins that experienced multiple extensional phases followed by post-extensional thermal subsidence.

Author contribution

M. Warsitzka designed and performed analogue experiments under guidance of Nina Kukowski and Jonas Kley. The manuscript was written by Michael Warsitzka with contributions and ideas by Jonas Kley and Nina Kukowski.

Appendix A:

A1 Frictional – plastic material behaviour

The mechanical behaviour of granular material like sand is described by the coefficient of internal friction μ and the cohesion C (Lohrmann et al., 2003). These material properties were measured in two-cycle dynamic friction tests at variable normal loads and variable shear rates with the ring-shear tester RST-01.pc (Schulze, 1994). During

SED
6, 1625–1686, 2014

a first shear load cycle, peak friction was determined, which defines the strength during material failure and shear zone formation. In a second shear load cycle, the static stable frictional strength was measured, which represents the strength during reactivation shear zones within the material. Following material failure after exceeding peak strength or static stable strength, respectively, a constant dynamic-stable strength in a stage of ongoing fault activity is reached (Panien et al., 2006).

The values of average frictional properties and bulk density of the materials used in our experiments are listed in Table A1. Similar to our experimental procedure sand was sifted in the measurements of the ring shear tests to achieve optimal grain package (Lohrmann et al., 2003). Applying the sieving procedure the densities of the granular materials vary in the order of $\Delta\rho = 30\,\mathrm{kg\,m^{-3}}$ (Table A1). Accuracy of the estimation of cohesion is quite low ($\sim 50\,\%$). Due to electrostatic forces, the cohesions of pure PVC-beads might be significantly higher, especially under tension. Nevertheless, the mixture of PVC beads and quartz sand visibly reduces electrostatic accumulation of the particles.

A2 Viscoelastic material behaviour

The silicone oil (Polydimethylsiloxane; Momentive Performance Materials Baysilone® SE30) used in our experiments is characterized by a power-law viscous rheology. In creep and relaxation tests a low power-law stress exponent of $n = 1.3$ had been determined by Rosenau et al. (2009) for the same silicone material used in our study. Additionally, we measured the viscosity with a cone-plate rheometer RC20.1-CPS-P1 with C25-2 measurement system (RheoTec). During measurement a thin film of silicone is sheared between the plates of the rheometer at controlled shear rates and room temperature (20 °C). The viscosity is calculated as the ratio of measured shear stress and strain rate. Thickness of the silicone film has been increased stepwise from 1 to 3 mm. Measurements have been repeated 3 times for each thickness. Average values for viscosity are listed in Table A2.

SED
6, 1625–1686, 2014

In order to record material movement with PIV, the transparent silicone was mixed with PVC beads. The viscosity of the mixed silicone is only slightly higher ($\Delta\eta$ = 240 Pa s) than that of pure silicone (Table A2). The bulk density of the mixed silicone remains unaffected since the PVC beads possess a similar grain density compared to the density of pure silicone.

Appendix B:

To ensure significance of experimental results, experiments have to be properly scaled geometrically, kinematically and dynamically. Models are considered as geometrically scaled, if ratios of linear dimensions in the model are proportionally similar to length ratios in nature (Hubbert, 1937). We used a length ratio l^* between model and nature of 10^{-5} (1 cm in the model corresponds to 1 km in nature), which is derived from the ratio of cohesion of the brittle cover (e.g. Koyi et al., 1993; Nalpas and Brun, 1992; Vendeville et al., 1995; Weijermars et al., 1993):

$$l^* = \left(C_0/g\rho\right)^* \tag{B1}$$

in which C_0 is the cohesion, g the gravitational acceleration, ρ the density and * represents the ratio between model and nature. Kinematic scaling is achieved, if the ratios between strain and time are similar for model and nature (Hubbert, 1937). The time ratio considers the viscosity ratio η^* between the silicone and the rock salt and the stress ratio σ^* (Table 1):

$$t^* = (\eta^*/\sigma^*) \tag{B2}$$

Since we simulate a tensile stress regime, lithostatic pressure is the main principal stress (Twiss and Moores, 1992):

$$\sigma_N = g \cdot \rho_b \cdot h_b \tag{B3}$$

SED
6, 1625–1686, 2014

Here, g is the gravitational acceleration, ρ_b the bulk density and h_b the thickness of the salt cover layer. Implying values for viscosities, length and density of Table 1, the time ratio becomes $t^* = \sim 1.3 \times 10^{-9}$. Consequently, one hour in experiments equals approximately 1 Ma. The strain rate ratio $\varepsilon^*(\varepsilon_m/\varepsilon_n)$ is inverse of time ratio $1/t^*$.

In order to fulfil dynamic scaling, the strength ratio between brittle cover S_b and ductile layer S_d has to be equal for nature and experiment (Weijermars et al., 1993). S_b equals the differential stress between maximum and minimum principal stresses:

$$S_b = \sigma_1 - \sigma_3 \tag{B4}$$

As mentioned above, the maximal principal stress σ_1 equals the overburden pressure due to gravity σ_N, whereas the minimal principal stress σ_3 is horizontal and in direction of extension. Both, natural sediment and granular analogue material are supposed to deform according to the Mohr–Coulomb failure criterion which is given by (Byerlee, 1978; Dahlen, 1990):

$$\tau_m = \sigma_m \sin\phi + C_0 \cos\phi \tag{B5}$$

in which σ_m = normal stress, τ_m = shear stress, ϕ is the angle of internal friction and C_0 the cohesion. Translating to an expression of maximum and minimum stresses gives:

$$\frac{\sigma_1 - \sigma_3}{2} = \frac{\sigma_1 + \sigma_3}{2} \sin\phi + C_0 \cos\phi \tag{B6}$$

With separation of σ_3, one obtains:

$$\sigma_3 = -\sigma_1 \frac{(1 - \sin\phi)}{(1 + \sin\phi)} + 2C_0 \sqrt{\frac{(1 - \sin\phi)}{(1 + \sin\phi)}} \tag{B7}$$

Finally, brittle strength S_b can be expressed by:

$$S_b = \sigma_1 + \sigma_1 \frac{(1 - \sin\phi)}{(1 + \sin\phi)} - 2C_0 \sqrt{\frac{(1 - \sin\phi)}{(1 + \sin\phi)}} \tag{B8}$$

SED
6, 1625–1686, 2014

For upper crustal rocks, a suitable value for angle of internal friction is $\phi = 30^\circ$ and for cohesion is $C_0 = 5 \times 10^6$ Pa (Byerlee, 1978). Generally, density of clastic sediments usually exceeds the density of rock salt (of $\rho_{Salt} = 2200\,kg\,m^3$) at depths of 650 to 1500 m (Baldwin and Butler, 1985). Assuming a pre-kinematic cover thickness of h_b = 1000 m we applied a cover density of $\rho_b = 2300\,kg\,m^3$ for the calculation (Baldwin and Butler, 1985). Therefore, $\sigma_N = \sigma_1 = 2.26 \times 10^7$ Pa and $\sigma_3 = 0.297 \times 10^7$ Pa. Hence, the brittle yield strength at the base is S_b(nature) = 1.96×10^7 Pa.

The mixture of quartz sand and PVC beads possesses a slightly lower angle of internal friction ($\phi = \sim 27^\circ$). In return, the density contrast between granulate and silicone ($\Delta\rho = 300\,kg\,m^{-3}$) is only slightly higher than the natural salt-cover density contrast, which is an advance compared to previous analogue models using pure quartz sand ($\Delta\rho$ = 500–700 $kg\,m^{-3}$). Using values of Table 1 S_b(model) = 60–160 Pa.

Shear stresses in a Newtonian fluid can be calculated by (Turcotte and Schubert, 2002):

$$S_d = \eta \left(u \Big/ \frac{1}{2} h_d \right) \tag{B9}$$

in which η is dynamic viscosity, u the displacement rate and h_d the thickness of the viscous layer. The extension rate for continental rifting varies between 0.1 and 1 mm a^{-1} (Allen and Allen, 2005), which gives strain rates in the viscous layer of $\varepsilon = 10^{-14}$ to $10^{-15}\,s^{-1}$ for a salt thickness of 2000 m. Assuming an average viscosity for natural rock salt of $\eta = 10^{18}$ Pa s (Nalpas and Brun, 1993; van Keken et al., 1993) and a salt thickness of 2000 m, S_d(nature) = 10^4–10^5 Pa.

In our experiments, the displacement rate of the simulated basement extension is $e = 4\,mm\,h^{-1}$ (except of one experiment with $e = 0.6\,mm\,h^{-1}$ and another experiment with $e = 20\,mm\,h^{-1}$, Table 2). Consequently, strain rates in the viscous layer reach values of $\varepsilon = \sim 10^{-5}\,s^{-1}$. Incorporating a silicone layer of a thickness of h_d = 1.5 cm and a viscosity of $\eta = 2.3 \times 10^4$ Pa s, S_d(model) = ~ 1 Pa.

SED
6, 1625–1686, 2014

The dimensionless strength ratios are calculated by:

S_b/S_d(nature) =~ 100–1000

and

S_b/S_d(model) = 50–180.

The model ratio lies within the lower range of the natural ratio. Hence, the models can be presumed as dynamically scaled.

The Supplement related to this article is available online at doi:10.5194/sed-6-1625-2014-supplement.

Acknowledgements. This experimental study was funded by the German Research Foundation (DFG). Experiments and measurements of material properties were carried out at the Helmholtz Centre Potsdam GFZ German Research Centre for Geosciences. We thank the GFZ technicians for assistance in the laboratory as well as M. Rosenau (GFZ Potsdam), M. Scheck-Wenderoth (GFZ Potsdam), and F. Jähne (Federal Institute for Geosciences and Natural Resources Hannover, BGR) for constructive discussions.

References

Adam, J., Urai, J. L., Wieneke, B., Oncken, O., Pfeiffer, K., Kukowski, N., Lohrmann, J., Hoth, S., van der Zee, W., and Schmatz, J.: Shear localisation and strain distribution during tectonic faulting – new insights from granular-flow experiments and high-resolution optical image correlation techniques, J. Struct. Geol., 27, 283–301, doi:10.1016/j.jsg.2004.08.008, 2005.

Allen, P. A. and Allen, J. R.: Basin Analysis Principles & Applications, 2nd edn., Blackwell Science, 451 pp., 2005.

SED
6, 1625–1686, 2014

Allen, J. and Beaumont, C.: Impact of inconsistent density scaling on physical analogue models of continental margin scale salt tectonics, J. Geophys. Res., 17, 1–22, doi:10.1029/2012JB009227, 2012.
Alves, T. M., Gawthorpe, R. L., Hunt, D. W., and Monteiro, J. H.: Jurassic tectono-sedimentary evolution of the Northern Lusitanian Basin (offshore Portugal), Mar. Petrol. Geol., 19, 727–754, doi:10.1046/j.1365-2117.2003.00202.x, 2002.
Baldschuhn, R., Binot, F., Frisch, U., and Kockel, F.: Geotektonischer Atlas von Nordwest-Deutschland und dem deutschen Nordsee-Sektor – Strukturen, Strukturentwicklung, Paläogeographie (Tectonic Atlas of Northwest Germany and the German North Sea Sector), Geologisches Jahrbuch A 153, 3 CD-ROM, 88 pp., 2001.
Baldwin, B. and Butler, C. O.: Compaction curves, AAPG Bull., 69, 622–626, 1985.
Bornemann, O.: Das Gefügeinventar nordwestdeutscher Salzstrukturen in Abhängigkeit von ihrer halokinetischen Stellung, Universitaet Braunschweig, Dissertationen, Braunschweig, 1–119, 1979.
Boutelier, D., Schrank, C., and Cruden, A.: Power-law viscous materials for analogue experiments: new data on the rheology of highly-filled silicone polymers, J. Struct. Geol., 30, 341–353, doi:10.1016/j.jsg.2007.10.009, 2008.
Burliga, S.: Implications for early basin dynamics of the Mid-Polish Trough from deformational structures within salt deposits in central Poland, Geol. Quart., 40, 185–202, 1996.
Burliga, S., Koyi, H. A., and Chemia, Z.: Analogue and numerical modelling of salt supply to a diapiric structure rising above an active basement fault, in: Salt Tectonics, Sediments and Prospectivity, edited by: Alsop, G. I., Archer, S. G., Hartley, A. J., Grant, N. T., and Hodgkinson, R., Geol. Soc. Spec. Publ., 363, 395–408, doi:10.1144/SP363.18, 2012.
Byerlee, J. D.: Friction of rocks, in: Pure and Applied Geophysics, edited by: Byerlee, J. D. and Wyss, M., Contribution to Current Research in Geophysics, 615–626, 1978.
Cobbold, P., Rossello, E., and Vendeville, B.: Some experiments on interacting sedimentation and deformation above salt horizons, B. Soc. Bull. Fr., 3, 453–460, doi:10.2113/gssgfbull.V.3.453, 1989.
Dadlez, R.: Mesozoic thickness pattern in the Mid-Polish Trough, Geol. Q., 47, 223–240, 2003.
Dahlen, F. A.: Critical Taper Model of Fold-And-Thrust Belts and Accretionary Wedges, Ann. Rev. Earth Pl. Sc., 18, 55–99, doi:10.1146/annurev.ea.18.050190.000415, 1990.

SED
6, 1625–1686, 2014

Dooley, T. P., McClay, P. R., and Pascoe, R.: 3-D analogue models of variable displacement extensional faults: applications to the Revfallet Fault system, offshore mid-Norway, Geol. Soc. Spec. Publ., 212, 151–167, doi:10.1144/GSL.SP.2003.212.01.10, 2003.

Dooley, T. P., McClay, K. R., Hempton, M., and Smit, D.: Salt tectonics above complex basement extensional fault systems: results from analogue modeling, in: Petroleum Geology: North-West Europe and Global Perspectives, Proceedings of the 6th Petroleum Geology Conference, edited by: Doré, A. G. and Vining, B. A., Geological Society, London, 1631–1648, doi:10.1144/0061631, 2005.

Duffy, O. B., Gawthorpe, R. L., Docherty, M., and Brocklehurst, S. H.: Mobile evaporite controls on the structural style and evolution of rift basins: Danish Central Graben, North Sea, Basin Res., 25, 310–330, doi:10.1111/bre.12000, 2013.

Frisch, U. and Kockel, F.: Quantification of Early Cimmerian movements in NW-Germany, Zbl. Geo. Pal., 7–8, 571–600, 1999.

Gaullier, V., Brun, J. P., and Lecanu, H.: Raft tectonics: the effects of residual topography below a salt décollement, Tectonophysics, 228, 363–381, doi:10.1016/0040-1951(93)90349-O, 1993.

Ge, H. and Vendeville, B. C.: Influence of active subsalt normal faults on the growth and location of suprasalt structures, Gulf Coast Association of Geological Societies Transactions, XLVII, 169–176, 1997.

Geil, K.: The development of salt structures in Denmark and adjacent areas: the role of basin floor dip and differential pressure, First Break, 9, 467–483, doi:10.3997/1365-2397.1991022, 1991.

Geluk, M. C.: Stratigraphy and tectonics of Permo-Triassic basins in the Netherlands and surrounding areas, Thesis, Univ. Utrecht, 1–171, 2005.

Goteti, R., Ings, S. J., and Beaumont, C.: Development of salt minibasins initiated by sedimentary topographic relief, Earth Planet. Sc. Lett., 339, 103–116, doi:10.1016/j.epsl.2012.04.045, 2012.

Higgins, R. I. and Harris, L. B.: The effect of cover composition on extensional faulting above re-activated basement faults: results from analogue modelling, J. Struct. Geol., 19, 89–98, doi:10.1016/S0191-8141(96)00083-1, 1997.

Hubbert, M. K.: Theory of scale models as applied to the study of geologic structures, Geol. Soc. Am. Bull., 48, 1459–1520, 1937.

SED
6, 1625–1686, 2014

Hudec, M. R. and Jackson, M. P. A.: Terra infirma: understanding salt tectonics, Earth Sci. Rev., 82, 1–27, doi:10.1016/j.earscirev.2007.01.001, 2007.
Hudec, M. R. and Jackson, M. P. A.: The Salt Mine: a Digital Atlas of Salt Tectonics, Bureau of Economic Geology Udden Book Series No. 5, AAPG Memoir, 99 pp., 2011.
Jackson, M. P. A. and Talbot, C. J.: External shapes, strain rates, and dynamics of salt structures, Geol. Soc. Am. Bull., 97, 305–323, doi:10.1130/0016-7606(1986)97<305:ESSRAD>2.0.CO;2, 1986.
Jackson, M. P. A. and Vendeville, B. C.: Regional extension as a geologic trigger for diapirism, Geol. Soc. Am. Bull., 94, 57–73, doi:10.1130/0016-7606(1994)106<0057:REAAGT>2.3.CO;2, 1994.
Jackson, M. P. A., Vendeville, B. C., and Schultz-Ela, D. D.: Structural Dynamics of Salt Systems, Ann. Rev. Earth Pl. Sc., 22, 93–117, doi:10.1146/annurev.ea.22.050194.000521, 1994.
Jaritz, W.: The origin and development of salt structures in Northwest Germany, in: Dynamical Geology of Salt and Related Structures, edited by: Lerche, I. and O'Brian, J. J., Academic Press, Orlando, FL, 479–493, 1987.
Kehle, R. O.: The origin of salt structures, in: Evaporites and Hydrocarbons, edited by: Schreiber, B. C., Columbia University Press, New York, 345–404, 1988.
Kockel, F.: Salt problems in NW-Germany and the German North Sea Sector, J. Seism. Explor., 7, 219–235, 1998.
Kockel, F.: Rifting processes in NW-Germany and the German North Sea Sector, Neth. J. Geosci.-Geol. Mijnbouw, 81, 149–158, 2002.
Korstgård, J. A., Lerche, I., Mogensen, T. E., and Thomsen, R. O.: Salt and fault interactions in the northeastern Danish Central Graben: observations and inferences, Bull. Geol. Soc. Den., 40, 197–255, 1993.
Kossow, D. and Krawczyk, C. M.: Structure and quantification of processes controlling the evolution of the inverted NE-German Basin, Mar. Petrol. Geol., 19, 601–618, doi:10.1016/S0264-8172(02)00032-6, 2002.
Koyi, H. A. and Petersen, K.: Influence of basement faults on the development of salt structures in the Danish Basin, Mar. Petrol. Geol., 10, 82–94, doi:10.1016/0264-8172(93)90015-K, 1993.
Koyi, H. A., Jenyon, M. K., and Petersen, K.: The effect of basement faulting on diapirism, J. Petrol. Geol., 163, 285–311, doi:10.1111/j.1747-5457.1993.tb00339.x, 1993.

SED
6, 1625–1686, 2014

Krzywiec, P.: Basement vs. salt tectonics and salt-sediment Interaction – case study of the Mesozoic evolution of the Intracontinental Mid-Polish Trough, in: 24th Annual GCSSEPM Foundation Bob F. Perkins Research Conference Salt-Sediment Interactions and Hydrocarbon Prospectivity: Concepts, Applications and Case Studies for the 21st Century, Houston, Texas, 2004a.

Krzywiec, P.: Triassic evolution of the Klodawa salt structure: basement-controlled salt tectonics within the Mid-Polish Trough (Central Poland), Geol. Quart., 48, 123–134, 2004b.

LaVision, Anon.: StrainMaster Manual for DaVis 6.2, LaVision GmbH, Göttingen, 2002.

Lohrmann, J., Kukowski, N., Adam, J., and Oncken, O.: The impact of analogue material parameters on the geometry, kinematics, and dynamics of convergent sand wedges. J. Struct. Geol., 25, 1691–1711,doi:10.1016/S0191-8141(03)00005-1, 2003.

Maystrenko, Y. P., Bayer, U., and Scheck-Wenderoth, M.: Salt as a 3-D element in structural modeling – Example from the Central European Basin System, Tectonophysics, 591, 62–82, doi:10.1016/j.tecto.2012.06.030, 2013.

Mohr, M., Kukla, P. A., Urai, J. L., and Bresser, G.: Multiphase salt tectonic evolution in NW Germany: seismic interpretation and retro-deformation, Int. J. Earth Sci., 94, 917–940, doi:10.1007/s00531-005-0498-8, 2005.

Nalpas, T. and Brun, J. P.: Salt flow and diapirism related to extension at crustal scale, Tectonophysics, 228, 349–362, doi:10.1016/0040-1951(93)90348-N, 1993.

Oudmayer, B. C. and de Jager, J.: Fault reactivation and oblique-slip in the Southern North Sea, in: Petroleum Geology of Northwest Europe: Proceedings of the 4th Conference, Petroleum Geology '86 Ltd, edited by: Parker, J. R., published by The Geological Society, London, 1281–1290, doi:10.1144/0041281, 1993.

Panien, M., Schreurs, G., and Pfiffner, A.: Mechanical behaviour of granular materials used in analogue modelling: insights from grain characterisation, ring-shear tests and analogue experiments, J. Struct. Geol., 28, 1710–1724, doi:10.1016/j.jsg.2006.05.004, 2006.

Ramberg, H.: Gravity Deformation and the Earth's Crust, 1st edn., Academic Press, London, 1967.

Remmelts, G.: Fault-related tectonics in the Southern North Sea, the Netherlands, in: Salt Tectonics: a Global Perspective, edited by: Jackson, M. P. A., Roberts, D. G., and Snelson, S., AAPG Memoir, 65, 261–272, 1995.

SED
6, 1625–1686, 2014

Richard, P.: Experiments on faulting in a two-layer cover sequence overlying a reactivated basement fault with oblique-slip, J. Struct. Geol., 13, 459–469, doi:10.1016/0191-8141(91)90018-E, 1991.
Richter-Bernburg, G.: Salt tectonics, interior structures of salt bodies, Bull. Cent. Rech. Explor.-Prod. Elf-Aquitaine, 4, 373–393, 1980.
Rosenau, M., Lohrmann, J., and Oncken, O.: Shocks in a box: an analog model of subduction earthquake cycles with application to seismotectonic forearc evolution, J. Geophys. Res., 114, 1978–2012, doi:10.1029/2008JB005665, 2009.
Rowan, M. G. and Ratliff, R. A.: Cross-section restoration of salt-related deformation: best practices and potential pitfalls, J. Strut. Geol., 41, 24–37, doi:10.1016/j.jsg.2011.12.012, 2012.
Scheck, M., Bayer, U., and Lewerenz, B.: Salt movements in the Northeast German Basin and its relation to major post-Permian tectonic phases – results from 3-D structural modelling, backstripping and reflection seismic data, Tectonophysics, 361, 277–299, doi:10.1016/S0040-1951(02)00650-9, 2003.
Scheck-Wenderoth, M., Maystrenko, Y. P., Hübscher, C., Hansen, M., and Mazur, S.: Dynamics of salt basins, in: Dynamics of complex intracontinental basins: the Central European Basin System, edited by: Littke, R., Bayer, U., Gajewski, D., Frontiers in Earth Science, Springer, Berlin, 2008.
Schultz-Ela, D. D. and Jackson, M. P. A.: Relation of subsalt structures to suprasalt structures during extension, AAPG Bull., 80, 1896–1923, 1996.
Schulze, D.: Entwicklung und Anwendung eines neuartigen Ringschergerätes, Aufbereitungstechnik, 35, 524–535, 1994.
Sørensen, K.: The salt pillow to diapir transition: evidence from unroofing unconformities in the Norwegian–Danish Basin, Petrol. Geosci., 4, 193–202, 1998.
Soto, R., Casas-Sainz, A., Del Río, P.: Geometry of half-grabens containing a mid-level viscous décollement, Basin Res., 19.3, 437–450, doi:10.1111/j.1365-2117.2007.00328.x, 2007.
Stephansson, O.: Theoretical and experimental studies of diapiric structures on Öland, Geol. Inst. Bull. Univ. Uppsala N.S., 3, 163–200, 1972.
Stewart, S. A.: Salt tectonics in the North Sea Basin: a structural style template for seismic interpreters, Geol. Soc. Spec. Publ., 272, 361–396, doi:10.1144/GSL.SP.2007.272.01.19, 2007.

SED
6, 1625–1686, 2014

Stewart, S. A., Harvey, M. J., Otto, S. C., and Weston, P. J.: Influence of salt on fault geometry: examples from the UK salt basins, Geol. Soc. Spec. Publ., 100, 175–202, doi:10.1144/GSL.SP.1996.100.01.12, 1996.
Stovba, S. M. and Stephenson, R. A.: Style and timing of salt tectonics in the Dniepr-Donets Basin (Ukraine): implications for triggering and driving mechanisms of salt movement in sedimentary basins, Mar. Petrol. Geol., 19, 1169–1189, doi:10.1016/S0264-8172(03)00023-0, 2003.
Strozyk, F., van Gent, H., Urai, J. L., and Kukla, P. A.: 3-D seismic study of complex intra-salt deformation: an example from the Upper Permian Zechstein 3 stringer in the western Dutch offshore, Geol. Soc. Spec. Publ., 363, 489–501, doi:10.1144/SP363.23, 2013.
Strunck, P., Gaupp, R., and Steffan, M.: Early Triassic movement of Upper Permian (Zechstein) salt in Northwest Germany, Z. Geol. Paläont Teil, 1, Heft 7–8, 679–699, 1998.
Trusheim, F.: Mechanism of salt migration in Northern Germany, AAPG Bull., 44, 1519–1540, 1960.
Turcotte, D. L. and Schubert, G.: Geodynamics, 2nd edn., Cambridge University Press, Cambridge, UK, 2002.
Twiss, R. J. and Moores, E. M.: Structural Geology, W. H. Freeman and Company, Oxford, 1992.
Urai, J., Schléder, Z., Spiers, C., and Kukla, P.: Flow and transport properties of salt rocks, in: Dynamics of Complex Intracontinental Basins: the Central European Basin System, edited by: Littke, R., Bayer, U., Gajewski, D., and Nelskamp, S., 291–304, Springer, Berlin, Heidelberg, 2008.
Van Gent, H., Urai, J. L., and de Keijzer, M.: The internal geometry of salt structures – a first look using 3-D seismic data from the Zechstein of the Netherlands, J. Struct. Geol., 1–20, doi:10.1016/j.jsg.2010.07.005, 2010.
Van Keken, P. E., Spiers, C. J., van den Berg, A. P., and Muyzert, E. J.: The effective viscosity of rock salt: implementation of steady-state creep laws in numerical models of salt diapirism, Tectonophysics, 225, 457–476, doi:10.1016/0040-1951(93)90310-G, 1993.
van Wees, J.-D., Stephenson, R. A., Ziegler, P. A., Bayer, U., McCann, T., Dadlez, R., Gaupp, R., Narkiewicz, M., Bitzer, F., and Scheck, M.: On the origin of the Southern Permian Basin, Central Europe, Mar. Petrol. Geol., 17, 43–59, doi:10.1016/S0264-8172(99)00052-5, 2000.
Vendeville, B. C.: Scale models of basement-induced extension: Comptes Rendus de l'Academie des Sciences de Paris, 307, Serie II, 1013–1019, 1988.

SED
6, 1625–1686, 2014

Vendeville, B. C.: A new Interpretation of Trusheim's classic Model of Salt-Diapir-Growth, Gulf Coast Association of Geological Societies Transactions, 52, 953–952, 2002.
Vendeville, B. C. and Jackson, M. P. A.: The rise of diapirs during thin-skinned extension, Mar. Petrol. Geol., 9, 331–353, doi:10.1016/0264-8172(92)90047-I, 1992.
Vendeville, B. C., Ge, H., and Jackson, M. P. A.: Scale models of salt tectonics during basement-involved extension, Petrol. Geosci., 1, 179–183, doi:10.1144/petgeo.1.2.179, 1995.
Ventisette, C. D., Montanari, D., Bonini, M., and Sani, F.: Positive fault inversion triggering "intrusive diapirism": an analogue modelling perspective, Terra Nova, 17, 478–485, doi:10.1111/j.1365-3121.2005.00637.x, 2005.
Wagner, R., Leszczyñski, K., Pokorski, J., and Gumulak, K.: Palaeotectonic cross-sections through the Mid-Polish Trough, Geol. Q., 46(3), 293–306, 2002.
Warsitzka, M., Kley, J., and Kukowski, N.: Salt diapirism driven by differential loading – some insights from analogue modelling, Tectonophysics, 591, 83–97, doi:10.1016/j.tecto.2011.11.018, 2013.
Weijermars, R., Jackson, M. P. A., and Vendeville, B. C.: Rheological and tectonic modeling of salt provinces, Tectonophysics, 217, 143–174, doi:10.1016/0040-1951(93)90208-2, 1993.
Withjack, M. O. and Callaway, S.: Active normal faulting beneath a salt layer: an experimental study of deformation patterns in the cover sequence, AAPG Bull., 84, 627–651, 2000.
Ziegler, P. A.: Triassic Rifts and Facies Patterns in Western and Central Europe, Geol. Rundsch., 71, 747–772, doi:10.1007/BF01821101, 1982.

SED
6, 1625–1686, 2014

Table 1. Scaling parameters. Material properties (density, viscosity, friction and cohesion) are stated for analogue materials used in this experimental study (Appendix A).

Parameter	Sign	Dimension	Model	Nature	Scaling factor (model/nature)	Reference for natural values
geometric	l^*	[m]	0.01	1000	$\sim 10^{-5}$	
thickness (ductile layer)	h_d	[m]	0.01–0.02	1400–2500	10^{-5}	Kockel (2002); Maystrenko et al. (2013); Nalpas and Brun (1993); Scheck et al. (2003)
thickness (brittle layer)	h_b	[m]	0.003–0.015	600–1200	10^{-5}	Nalpas and Brun (1993)
kinematic						
strain	ε	–			1	–
time	t	[s]	100 h = 10^5 s	$\sim$ 30 Ma = $\sim 10^{15}$	10^{-10}	–
extension rate	u	[m s^{-1}]	10^{-6}	1 mm a^{-1} = $\sim 10^{-11}$ m s^{-1}	$\sim 10^5$	Allen and Allen (2005)
strain rate in viscous layer	ε'	[s^{-1}]	$\sim 10^{-5}$	10^{-11}–10^{-15}	10^{-6}–10^{-10}	Jackson and Talbot (1986); Nalpas and Brun (1993)
dynamic						
gravity acceleration	g	[m s^{-2}]	9.81	9.81	1	–
density (ductile layer)	ρ_d	[kg m^{-3}]	970	2200	0,44	Jackson and Talbot (1986)
density (brittle layer)	ρ_b	[kg m^{-3}]	1220	1800–2500	0.52–0.72	Jackson and Talbot (1986)
dynamic viscosity (ductile layer)	η	[Pa s]	2.3×10^4	10^{17}–10^{19}	$\sim 10^{-14}$	Nalpas and Brun (1993)
internal peak friction coefficient	μ	–	0.51 (±0.006)	0.5–0.6	1	Weijermars et al. (1993)
internal friction angle	ϕ	°	27	$\sim$ 30		Weijermars et al. (1993)
cohesion [Pa]	C_0	[Pa]	$\sim$ 100	5×10^6		Byerlee (1978)
stress and pressure		[Pa]			$\sim 10^{-5}$	–
brittle strength	S_b	[Pa]	60–160	$\sim 10^7$	$\sim 10^{-5}$	–
ductile strength	S_d	[Pa]	0.5–2	$\sim 10^5$	$\sim 10^{-5}$	–
Brittle strength/ductile strength	S/S_d	–	50–180	$\sim$ 100 – –1000	$\sim$ 1	–

SED
6, 1625–1686, 2014

Table 2. Experiments and key parameters, where h_d is the thickness of the ductile silicone and h_b the thickness of the brittle sand cover.

Experiment	h_d [cm]	h_b [cm]	Extension rate e [mm h^{-1}]	Subsidence d [mm]	Total duration [days]	PIV monitoring	Comment
1a	1.5	0.6	4	6	12	side view	–
1b	1.5	0.6	4	6 + 6	18	side view	2 phases of extension
1c	1.5	0.6	4	6	18	side view	erosion after 10 days
1d	1.5	0.6	4	6	4	side view + top view	–
2	1.5	0.6	20	6	4	side view	–
3	1.5	0.6	0.6	6	4	side view	–
4a	1	0.6	4	6	8	side view	–
4b	1	0.6	4	6	8	side view	sand accumulation during basement extension
5	2	0.6	4	6	9	side view	–
6	1.5	0.4	4	6	9	side view	–
7	1.5	1	4	6	5	side view	–
8	1.5	1.5	4	6	6	side view	–

SED
6, 1625–1686, 2014

Table A1. Material parameters (density ρ, coefficient of internal friction μ and the cohesion C) of used granular material measured with ring shear tester RST-01.pc.

Material	Grain size [mm]	Preparation	peak ρ [kg m^{-3}]	Peak μ	Peak C (Pa)	Stable static μ	Stable Static C (Pa)	Stable dynamic μ	Stable dynamic C (Pa)
PVC beads	0.36–0.5	sifted	750 ± 10	0.33 ± 0.006	109 ± 44	0.32 ± 0.003	119 ± 25	0.34 ± 0.030	121 ± 196
quartz sand G23	0.02–0.63	sifted	1740 ± 17	0.70 ± 0.008	88 ± 45	0.61 ± 0.005	92 ± 36	0.55 ± 0.002	103 ± 10
Mixture PVC : Quartz sand 1 : 1	0.02–0.63	sifted	1250 ± 10	0.51 ± 0.006	107 ± 44	0.50 ± 0.003	72 ± 25	0.45 ± 0.030	72 ± 196

SED
6, 1625–1686, 2014

Table A2. Physical properties of silicone putty used in the study presented here.

Material	Weight of sand added to silicone [kg]	Density ρ [kg m^{-3}]	Strain rate ε [s^{-1}]	Shear stresses τ [Pa]	Viscosity η [Pa s]
Silicone PDMS	0	970	0.01–0.08	< 2000	23 000 ± 1000
Silicone PDMS mixed with sand	0.01–0.03	970	0.01–0.08	< 2000	23 240 ± 1000

SED
6, 1625–1686, 2014

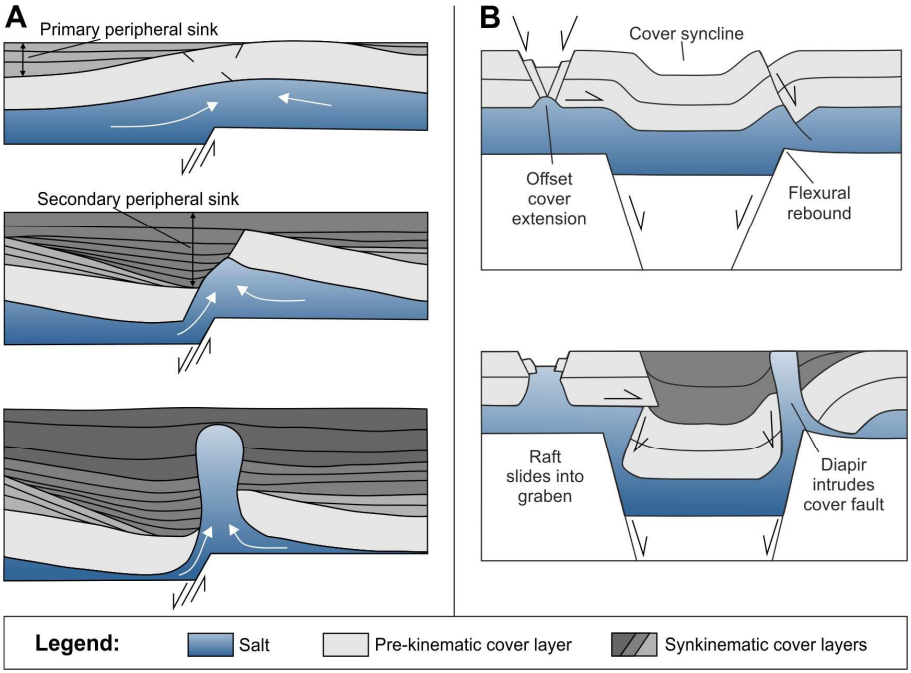

Figure 1. Conceptual models showing the evolution of salt diapirs induced by active basement faults. **(A)** Due to sedimentary loading a salt pillow develops prior to diapiric piercing (modified after Koyi et al., 1993). **(B)** Basement extension leads to faulting of the overburden and reactive diapirism (modified after Stewart, 2007). In both examples, salt flow is governed by differential loading due to basement subsidence and displacement loading due to cover faulting.

SED
6, 1625–1686, 2014

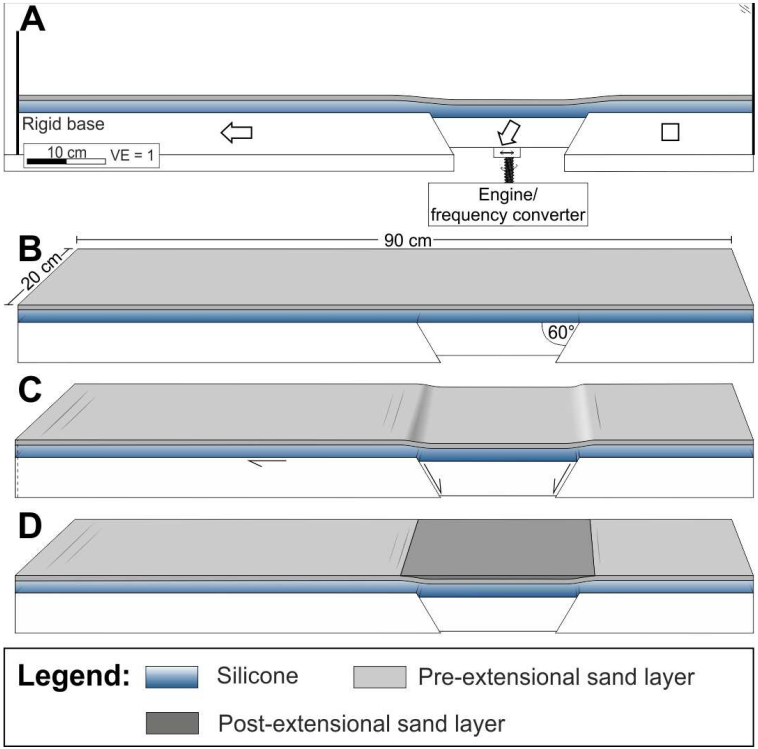

Figure 2. (A) Side view of experimental box comprising analogue materials silicone and granulate as well as subdivided rigid basement. Basal displacement is driven by controlled engine. **(B)** In general model procedure starts with planar layer configuration. **(C)** Basal displacement is applied. **(D)** Surface depressions are filled with sifted granulate. Sieving procedure is repeated daily.

SED
6, 1625–1686, 2014

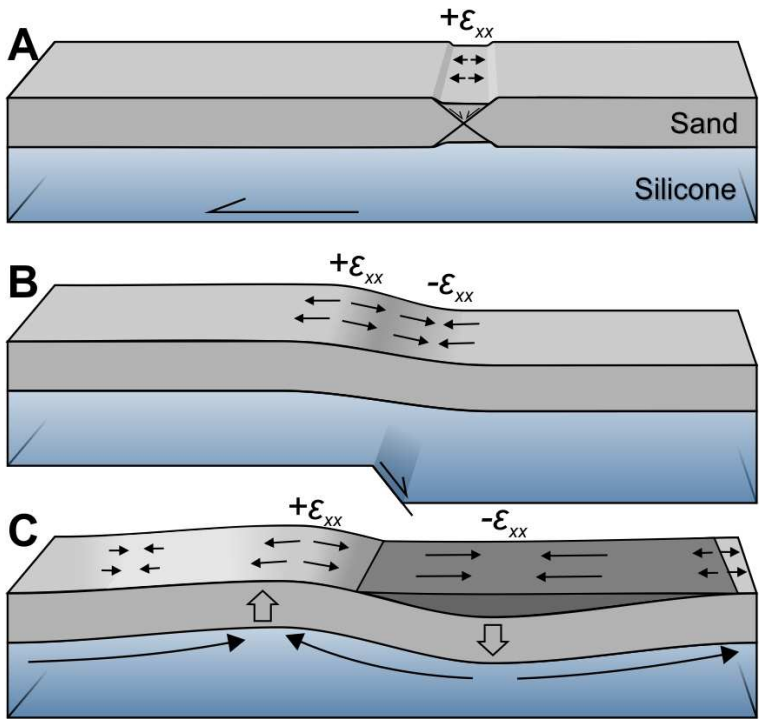

Figure 3. Explanation of horizontal strain observed with PIV in top-view (see results). **(A)** Cover extension, which is due to displacement of the basement, is measured as positive horizontal strain ($+\varepsilon_{xx}$). **(B)** Layer bending due to extensional forced folding is accompanied by extension ($+\varepsilon_{xx}$) and compression ($-\varepsilon_{xx}$) of the sand surface. **(C)** Similarly, surface uplift due to silicone inflation leads to crestal extension ($+\varepsilon_{xx}$). Surface subsidence due to silicone deflation causes compression ($-\varepsilon_{xx}$).

SED
6, 1625–1686, 2014

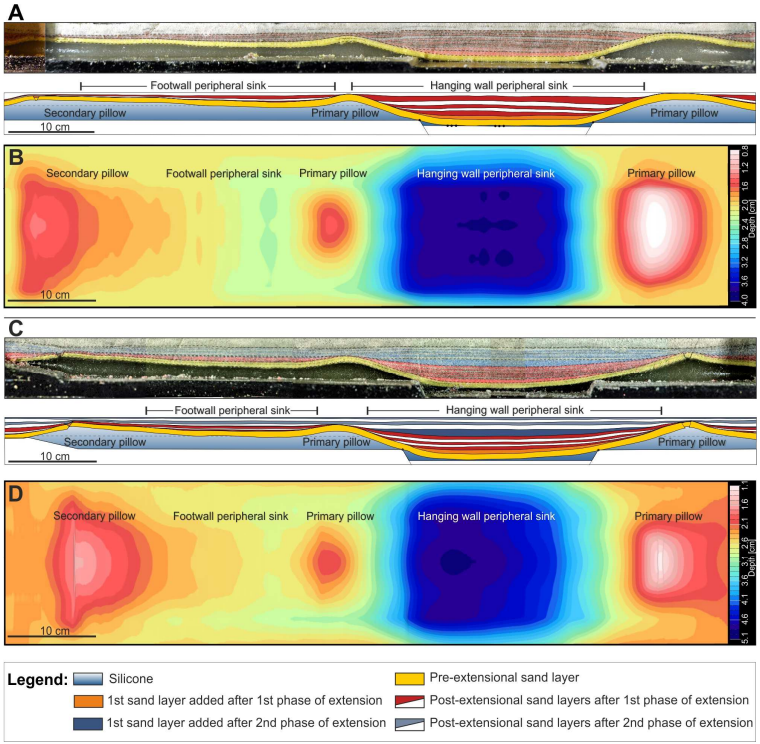

Figure 4. (A) Cross-section of reference experiment 1a after 12 days. Post-extensional strata reveals the hanging wall peripheral sink (HPS) enclosed by two pillow-like silicone elevations. Additional sinks as well as an additional secondary pillow occur on the left side of the box. **(B)** Colour map displaying the depth of the top of the silicone layer related to the final surface from Exp. 1a. The diameters of the pillows are smaller than the diameter of the HPS. **(C)** Cross-section of reference experiment 1b after 18 days, in which an additional phase of extension was applied after 10 days. The crests of the pillows are slightly faulted. **(D)** Depth map of the top of the silicone layer from Exp. 1b showing that the pillow structures are asymmetric.

SED
6, 1625–1686, 2014

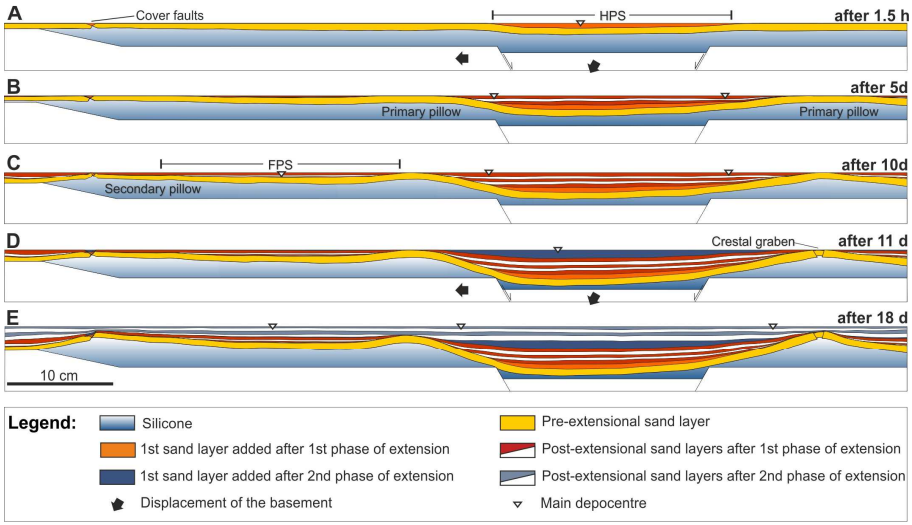

Figure 5. Restoration of final cross-section of Exp. 1b. **(A)** At the end of basement extension the hanging wall peripheral sink (HPS) formed. **(B)** Additional sand accumulated causes the formation of pillow structures close adjacent to downthrown basement block as well as above the platform at the left side of the box (secondary pillow). **(C)** The subsidence of the second phase of basement extension is marked by the dark blue layer. **(D)** Further post-extensional sand accumulation (blue/white) increases the elevation of the pillow-like structures.

SED
6, 1625–1686, 2014

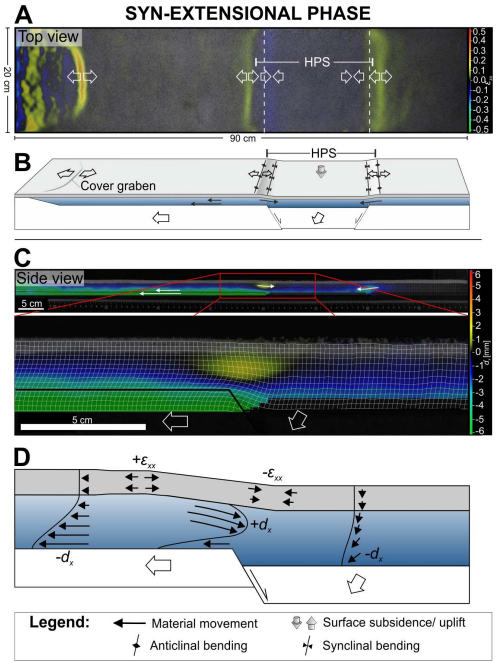

Figure 6. Results of PIV monitoring during syn-extensional phase of the reference experiment Exp. 1b and Exp. 1d. **(A)** Top view of Exp. 1d: horizontal strain ε_{xx} observed with PIV displaying zones of extension (yellow) and zones of compression (blue). Dashed lines indicate location of basal faults. HPS = hanging wall peripheral sink. **(B)** Sketch showing the interpretation of the PIV strain patterns. **(C)** Side view of Exp. 1b: horizontal displacement d_x observed with PIV including a detailed view of the left basement fault. Coloured areas display rightward (yellow-red) and leftward (green-blue) movement of the analogue material. **(D)** Conceptual sketch summarizing the interpreted displacement patterns and showing vector profiles representing the material movement. The viscous material above the fault tip flows towards the hanging wall side opposed to the shearing along the basement.

SED
6, 1625–1686, 2014

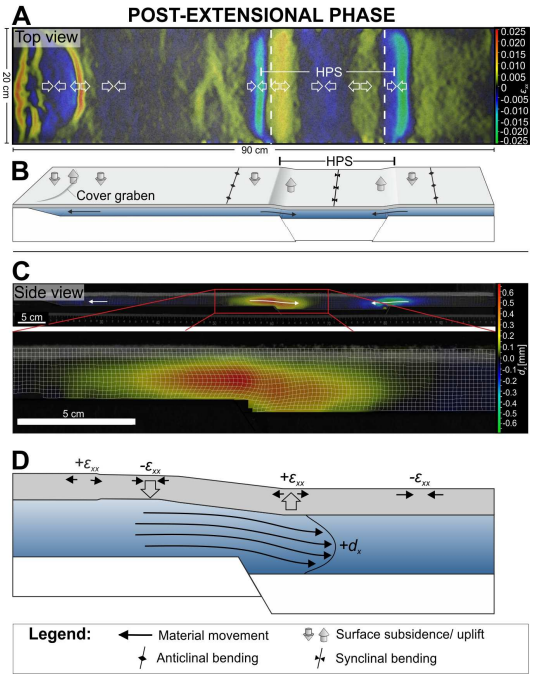

Figure 7. Results of PIV monitoring during the post-extensional phase of the reference experiment Exp. 1b and Exp. 1d 15 min after basement extension had ceased. **(A)** Top view of Exp. 1d: horizontal strain ε_{xx} observed with PIV displaying zones of extension (yellow) and zones of compression (blue). Dashed lines indicate location of basal faults. HPS = hanging wall peripheral sink. **(B)** Sketch showing the interpretation of the PIV strain patterns. **(C)** Side view of Exp. 1b: horizontal displacement d_x observed with PIV including a detailed view of the left basement fault. Coloured areas display rightward (yellow-red) and leftward (green-blue) movement of the analogue material. **(D)** Conceptual sketch summarizing the interpreted displacement patterns and showing representative vector profiles of the material movement.

SED
6, 1625–1686, 2014

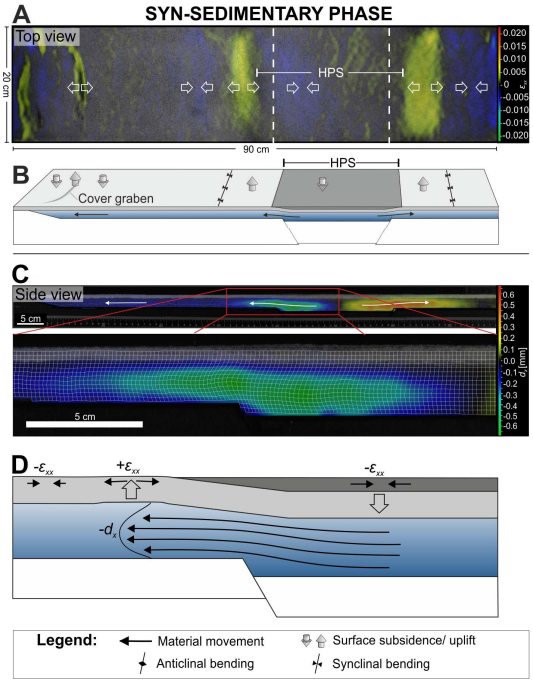

Figure 8. Results of PIV monitoring during syn-sedimentary phase of the reference experiment Exp. 1b and Exp. 1d 1 h after addition of the first post-extensional sand layer. **(A)** Top view of Exp. 1d: horizontal strain ε_{xx} observed with PIV displaying zones of extension (yellow) and zones of compression (blue). Dashed lines indicate location of basal faults. HPS = hanging wall peripheral sink. **(B)** Sketch showing the interpretation of the PIV strain patterns. **(C)** Side view of Exp. 1b: horizontal displacement d_x observed with PIV including a detailed view of the left basement fault. Coloured areas display rightward (yellow-red) and leftward (green-blue) movement of the analogue material. **(D)** Conceptual sketch summarizing the interpreted displacement patterns and showing representative vector profiles of the material movement.

SED
6, 1625–1686, 2014

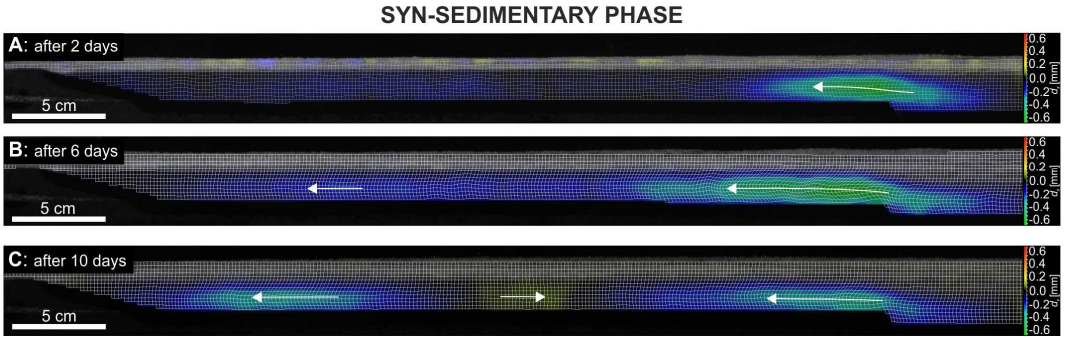

Figure 9. Time series of PIV displacement patterns of the reference experiment Exp. 1b during syn-sedimentary phase. **(A)** After 2 days, pronounced rightward (blue) directed movement occurs close to the basement fault tip. **(B)** After 6 days, the zone of rightward movement increases in width and additional flow appears apart from the basement fault. **(C)** After 10 days, significant displacement can be observed still above the basement fault as well as apart from the basement fault.

SED
6, 1625–1686, 2014

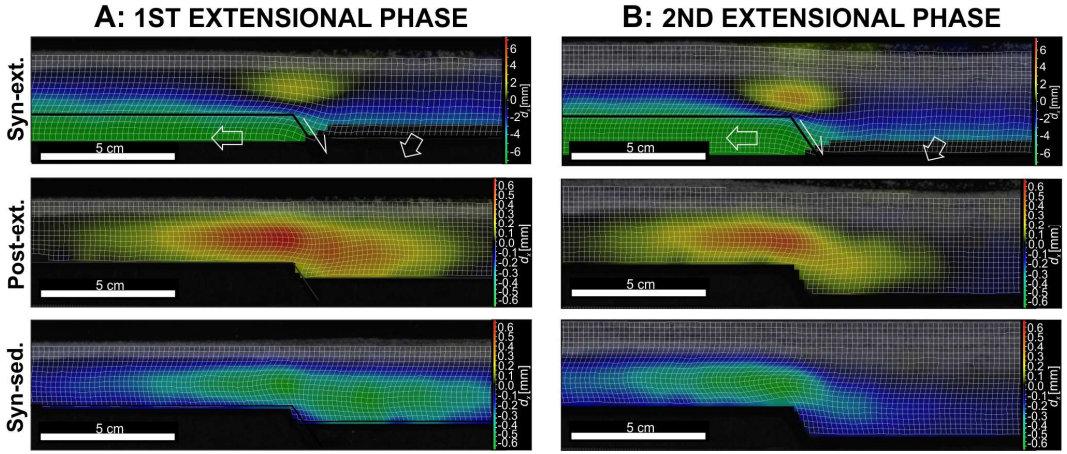

Figure 10. Comparison of horizontal displacement d_x in side-view above the tip of the basement fault during **(A)** first and **(B)** second phase of basement extension of the reference experiment Exp. 1b after 11 days of experimental duration. Coloured areas display rightward (yellow-red) and leftward (green-blue) movement of the analogue material.

SED
6, 1625–1686, 2014

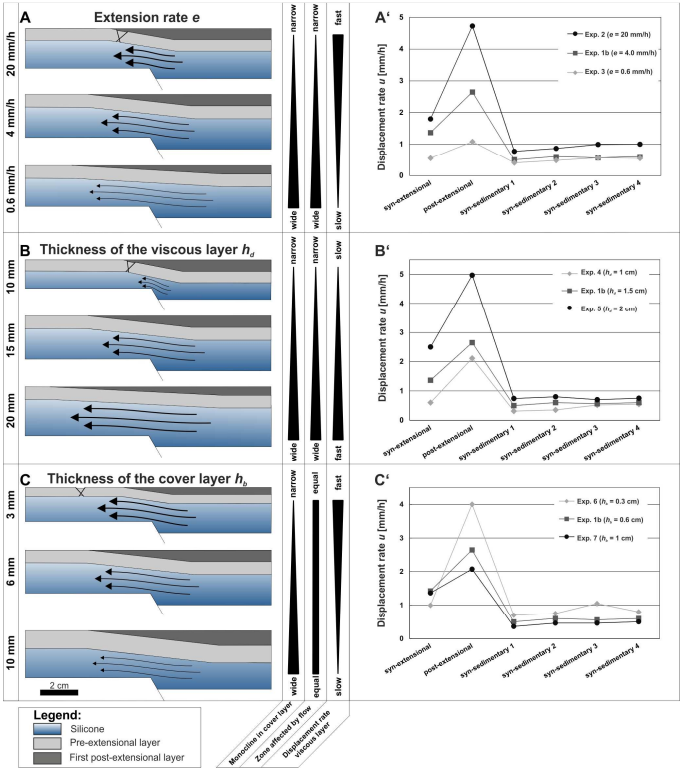

Figure 11. Summarized results of the structures, the kinematics, and the displacement rates u depending on (**A**/**A**′) extension rate at the basement fault e, (**B**/**B**′) thickness of the viscous layer h_d, and (**C**/**C**′) thickness of the cover layer h_b. Black arrows indicate extent of flow in the silicone layer, whereas the thickness of the arrows represents the displacement rates. Triangles and bars in the center column reflect increasing or decreasing effect on structures and kinematics. The displacement rates are generally highest during the post-extensional phase. During the syn-sedimentary phases, the displacement rates are notably lower. Note that only the values of the first 4 syn-sedimentary phases are displayed while most experiments last longer.

SED
6, 1625–1686, 2014

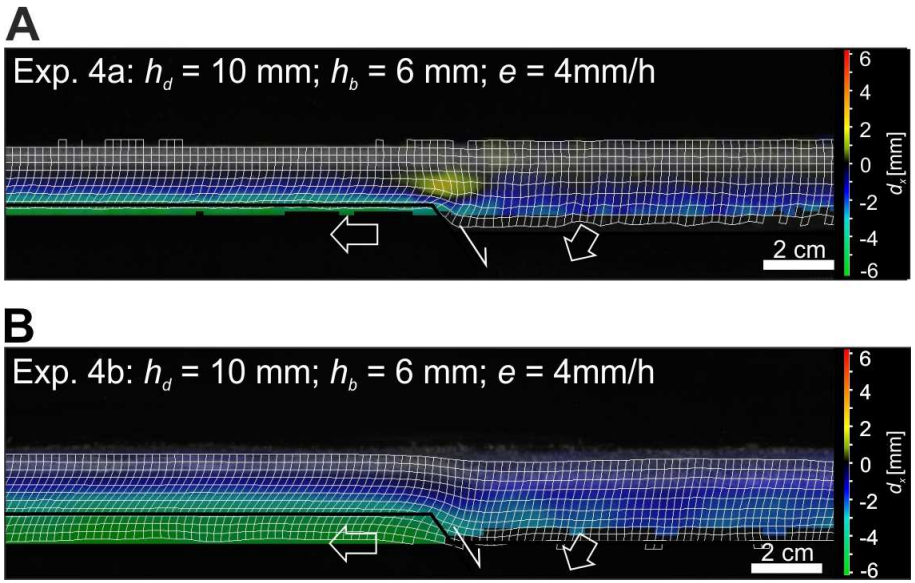

Figure 12. Comparison of two experiments with equal initial conditions, but **(A)** without syn-extensional sand accumulation and **(B)** with syn-extensional sand accumulation in the hanging wall peripheral sink. Downward flow is prevented in **(B)**. However, no upward flow can be recognized in **(B)**, although differential loading between the hanging wall side and the footwall side is present. Coloured areas display rightward (yellow-red) and leftward (green-blue) movement of the analogue material.

SED
6, 1625–1686, 2014

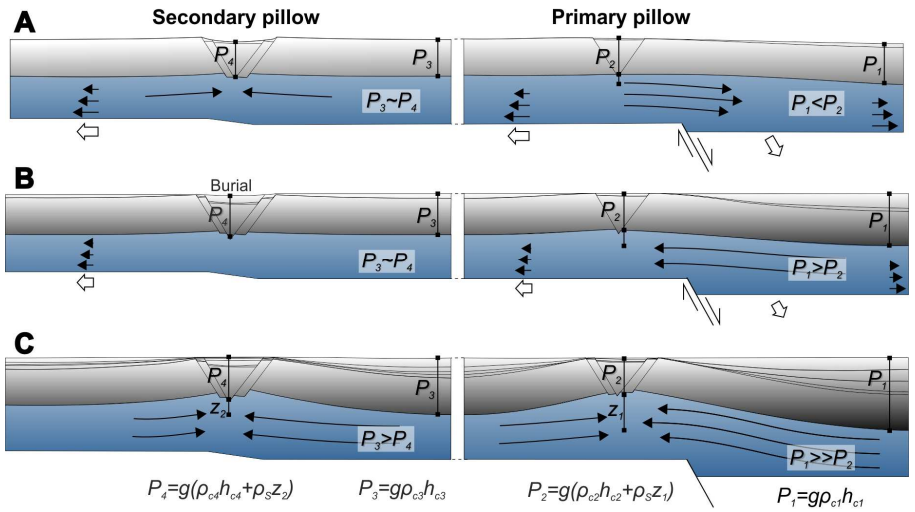

Figure 13. Conceptual model of the salt flow kinematics before and during the formation of a primary pillow next to the basement fault and a secondary pillow above the footwall block. The shading of the overburden layer represents an increasing density due to compaction. **(A)** During initiation of the basement fault downward flow occurs above the fault tip since pressure head is smaller than the elevation head. The formation of the secondary pillow is initiated by cover faulting and probably located by irregularities in the salt basement. **(B)** Due to further basement extension, thickness and density of the overburden above hanging wall side increase and loading differences in the overburden between the hanging wall block and the footwall block become more effective. Hence, upward flow above the basement fault is initiated. Meanwhile, the activity of the secondary pillow ceases due to burial. **(C)** During decreased or stopped extension, the salt continuously flows upward forming the primary pillow. The growth of the secondary pillow is enhanced by the formation of the footwall peripheral sink adjacent to the primary pillow.

SED
6, 1625–1686, 2014

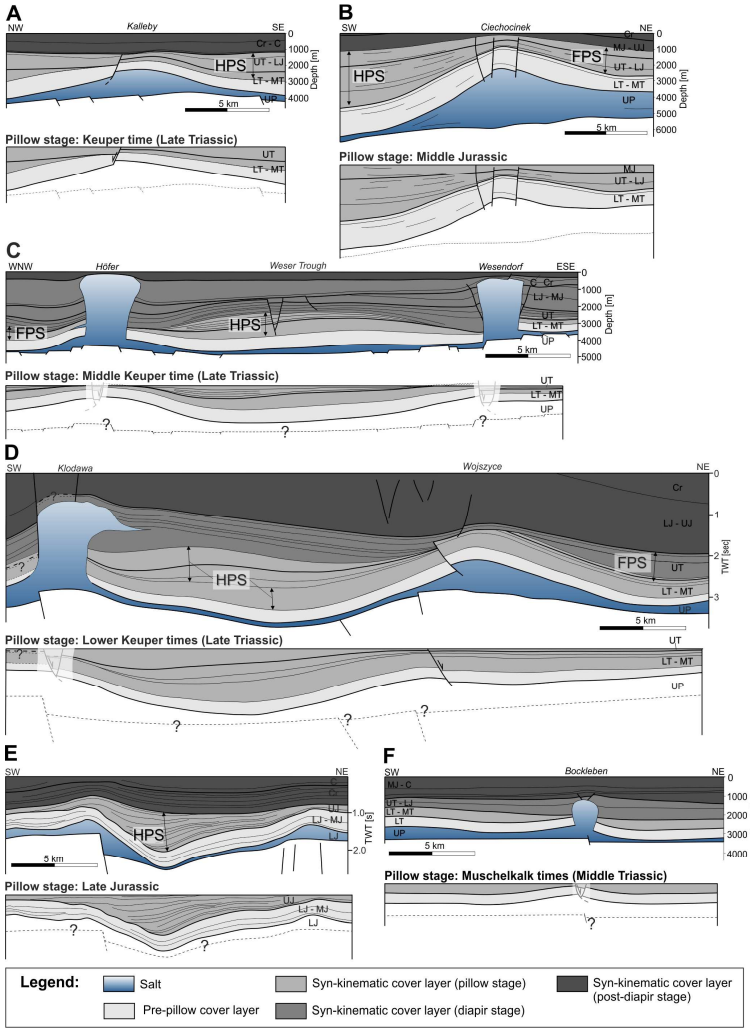

SED
6, 1625–1686, 2014

Analogue experiments of salt flow and pillow growth

M. Warsitzka et al.

Figure 14. Interpreted seismic profiles including reconstruction of the hanging wall peripheral sink (HPS) and the footwall peripheral sink (FPS). The subsalt basement has not been restored, whereby its geometry is schematically denoted. The cross-sections in **(A)** of the North German Basin (modified after Baldschuhn et al., 2001) and **(B)** of the Mid-Polish Basin (modified after Dadlez et al., 2003) show typical salt pillows that were initiated by differentially subsided basement. In cross-sections C–E, the main depocentres overlie the downthrown basement part and salt structures are situated above basement highs. **(C)** The Weser Trough (Central North German Basin) experienced several extensional phases during the Mesozoic, which led to the formation of salt pillows during Early Triassic and to diapiric piercing during Upper Triassic (modified from Baldschuhn et al., 2001). **(D)**: The salt structures Klodawa and Wojszyce in the Mid-Polish Trough were initiated during Middle to Late Triassic above a half graben (modified from Krzywiec, 2004b). Late Cretaceous inversion caused strong uplift of the sub-salt basement. **(E)**: In the Lusitanian Basins (offshore Portugal) a relatively thin salt layer evolved into small salt pillows during multiple extensional events from Early Jurassic to Early Cretaceous and was remobilized by basin inversion during the Tertiary (modified from Alves et al., 2002). **(F)** The salt structure Bockleben (North German Basin) likely started to grow as a secondary pillow above a small-offset basement fault during Middle Triassic (modified after Baldschuhn et al., 2001). UP – Upper Permian; LT – Lower Triassic; MT – Middle Triassic; UT – Upper Triassic, LJ – Lower Jurassic; MJ – Middle Jurassic; UJ – Upper Jurassic, Cr – Cretaceous; C – Cenozoic. For locations of the profiles see reference.

SED
6, 1625–1686, 2014